Progress in Surface Science 86 (2011) 328–376

Contents lists available at SciVerse ScienceDirect

Progress in Surface Science

journal homepage: www.elsevier.com/locate/progsurf

Review

Characterization of plasmonic effects in thin films and metamaterials using spectroscopic ellipsometry

T.W.H. Oates [a,*], H. Wormeester [b], H. Arwin [c]

[a] Leibniz-Institut für Analytische Wissenschaften – ISAS-Berlin, Albert-Einstein-Str., 9, D-12489 Berlin, Germany
[b] Physics of Interfaces and Nanomaterials, MESA+ Institute for Nanotechnology, University of Twente, 7522 NB Enschede, The Netherlands
[c] Laboratory of Applied Optics, IFM, Linköping University, SE-581 83 Linköping, Sweden

ARTICLE INFO

Commissioning Editor: H. Winter

Keywords:
Dielectric function
Permeability
Chirality
Near-field
SERS

ABSTRACT

In this article, spectroscopic ellipsometry studies of plasmon resonances at metal–dielectric interfaces of thin films are reviewed. We show how ellipsometry provides valuable non-invasive amplitude and phase information from which one can determine the effective dielectric functions, and how these relate to the material nanostructure and define exactly the plasmonic characteristics of the system. There are three related plasmons that are observable using spectroscopic ellipsometry; volume plasmon resonances, surface plasmon polaritons and particle plasmon resonances. We demonstrate that the established method of exploiting surface plasmon polaritons for chemical and biological sensing may be enhanced using the ellipsometric phase information and provide a comprehensive theoretical basis for the technique. We show how the particle and volume plasmon resonances in the ellipsometric spectra of nanoparticle films are directly related to size, surface coverage and constituent dielectric functions of the nanoparticles. The regularly observed splitting of the particle plasmon resonance is theoretically described using modified effective medium theories within the framework of ellipsometry. We demonstrate the wealth of information available from real-time *in situ* spectroscopic ellipsometry measurements of metal film deposition, including the evolution of the plasmon resonances and percolation events. Finally, we discuss how generalized and Mueller matrix ellipsometry hold great potential for characterizing plasmonic metamaterials and sub-wavelength hole arrays.

© 2011 Elsevier Ltd. All rights reserved.

* Corresponding author. Tel.: +49 30 6392 3554; fax: +49 30 6392 3544.
E-mail address: tom.oates@isas.de (T.W.H. Oates).

0079-6816/$ - see front matter © 2011 Elsevier Ltd. All rights reserved.
doi:10.1016/j.progsurf.2011.08.004

Contents

1. Introduction

In 1857, Michael Faraday provided a fascinating description of the various colours of colloidal suspensions and thin films of gold nanoparticles [1]. He presented results of the first detailed nanotechnology experiments, and discussed the phenomena which we now attribute to absorption and scattering of light by plasmon resonances. In fact, colloidal noble metal particles are found dispersed in beautifully coloured glass thousands of years old, the most prominent example being the Roman era Lycurgus cup [2]. In the last few decades the field of nano-optics has developed thanks to advances in nanoscale fabrication and physical phenomena based primarily on plasmons. The name "plasmonics" was originally coined in analogy with electronics [3] although the term is now broadly used to describe all plasmon-related optical research [4].

Like a tiny antenna, the electrons in a conductive nanoparticle resonate collectively, concentrating photonic energy into strongly localized electric fields at dimensions well below the diffraction limit. Exploiting these field enhancements, metallic nanoparticles are utilized to enhance chemical sensing [5], photovoltaic [6] and LED [7] efficiency. These collective electron oscillations, or plasmons, may also couple to a photon at a planar metal/dielectric interface, creating a surface plasmon polariton. The energy and geometry of the coupling are extremely sensitive to changes in the dielectric environment, leading to biological sensor elements termed surface plasmon resonance (SPR) sensors [8]. Recently, mesoscopic "artificial atoms" with defined plasmonic resonances have been used to design and build photonic metamaterials [9] displaying artificial magnetism and negative index of refraction.

Simultaneously with fabrication advances, nanotechnology has also progressed due to improved metrology. The accurate measurement of both particle sizes and their spectral resonances allows correlation of the optical and structural properties. Particle sizes are routinely measured in a small area of the sample using scanning probe and electron microscopy. In contrast, optical spectroscopy is usually performed by reflection or transmission measurements over a relatively large area. One observes the interaction of comparatively-long electromagnetic waves with charges and currents on the atomic scale. A statistical averaging of the microscopic properties is therefore a requirement of any mathematical analysis. The question has recently been posed as to how much useful information can be determined regarding the material nanostructure using macroscopic spectroscopy [10]. Obviously a technique that can simultaneously determine both the nanoscale structural and macroscopic optical properties of a material would be of great value.

This article aims to review the current status of ellipsometry, a sensitive polarized optical spectroscopy, in the context of plasmonics. While any discussion of ellipsometry is fundamentally related to the electromagnetic properties of materials, namely the permittivity and permeability discussed in Section 2, in this work we aim to describe other physical parameters that can be probed. From the Drude theory discussed in Section 3 one may link the optical measurements to the oscillations of bound and free electrons, from which one can determine the electrical conductivity, electron density and the mean free path of the electrons. By exciting plasmon waves on a metal surface one can probe the near surface region, of the order of a few nanometres, with extreme sensitivity, which has applications in the study of molecular absorption. We shall show in Section 4 that using ellipsometry provides additional phase information which increases the sensitivity yet further. Section 5 discusses the polarization of nanostructured metal elements which results in resonant absorption features in the optical spectra. The frequency, width and amplitude of these absorption curves depend on the particle density and shape, and the medium surrounding the metal. By applying effective medium theories one can determine these parameters from ellipsometry spectra, thereby providing nanostructural information from macroscopic measurements. In Section 6, we will show that applying Generalized and Mueller matrix ellipsometry to the study of plasmonic metamaterials has the potential to determine not only the dielectric and magnetic resonances of the artificial atoms, but also the permeability and permittivity tensors of anisotropic materials, including the gyrotropic tensors linking the electric and magnetic responses.

It is of historical interest to note that Paul Drude plays an important role in the establishment of both ellipsometry and the theory of metal optics on which plasmonics is based. Drude was an early champion of Maxwell's theory in Germany and developed the Drude model of metals, linking the

conductivity with the optical dispersion properties [11–14]. Drude experimentally demonstrated his theory using ellipsometry and, although its roots lie in the work of others in the decades prior [15], he is attributed with establishing the technique by laying the theoretical groundwork.

2. Spectroscopic ellipsometry

The polarization-dependence of plasmon resonances was observed by Wood in 1902, who surmised that "the results obtained with polarized light will be the means of eventually determining the exact cause of the colours" [16]. Spectroscopic ellipsometry is the measurement of polarized light reflected from a material surface or thin film in a configuration described as a "common-path polarization interferometer" [17]. From the measured quantities the optical properties and nanostructure of the materials may be calculated. Due to demanding measurement and calculation procedures, ellipsometry was historically applied in only the simplest of cases, primarily to determine the macroscopic optical properties of isotropic, homogeneous materials and thin films.

In the later part of last century, experimental ellipsometry was transformed by a number of technological advances, namely; the availability of computers to simplify the modelling process; instrument automation; multichannel spectral measurement; and extension of the measurement range to UV and infrared frequencies. Additionally, the mathematical models to handle the data analysis of anisotropic and depolarizing materials were developed and written into computer algorithms. For a detailed review of ellipsometry the reader is referred to the classic book of Azzam and Bashara [18] and also the contemporary works of Fujiwara [19], Schubert [20] and Tompkins and Irene [21]. To see what ellipsometry can tell us about the shape, size and electronic properties of nanostructured metals, first we need to consider what ellipsometry actually measures.

2.1. The dielectric function

To characterise the optical properties of a material we define parameters that relate the change in the electric and magnetic fields of light after reflection from, or transmission through, that material. Electromagnetic (EM) radiation causes a redistribution of the charges and currents in a material which is well described by the equations of Maxwell. The constitutive relations link the external electric and magnetic fields to the internal fields in the material, via the relative permittivity ε and permeability μ [22]

$$\mathbf{D} \equiv \varepsilon\varepsilon_0\mathbf{E} = \varepsilon_0\mathbf{E} + \mathbf{P} \tag{2.1}$$

$$\mathbf{B} \equiv \mu\mu_0\mathbf{H} = \mu_0\mathbf{H} + \mathbf{M} \tag{2.2}$$

where **E** and **B** are the electric and magnetic fields, **D** and **H** are the electric displacement and magnetic induction, **P** and **M** are the electric and magnetic polarizations, and ε_0 and μ_0 are the permittivity and permeability of vacuum, respectively. The solution to Maxwell's equations for an EM wave in an isotropic medium has electric and magnetic field transverse to the wave vector **k**, defined as $\mathbf{k} = k\mathbf{s}$, where **s** is the unit vector and $k = 2\pi/\lambda$, where λ is the wavelength of the light in the medium. The dispersion relation for transverse waves is

$$k^2 = \frac{\omega^2}{c^2}\varepsilon(\mathbf{k},\omega)\mu(\mathbf{k},\omega) \tag{2.3}$$

where c is the speed of light in a vacuum and ω is the angular frequency. In this work we will primarily use the photon energy, $\hbar\omega$, in units of eV.

For homogeneous materials it is convenient to assume that the wavelength is infinitely large, in which case $k \to 0$ and one may ignore any spatial frequency dependence. This assumption is valid for materials where the constituent units are much smaller than the light wavelength, such as atoms in the infrared and visible wavelength range. For very high frequencies (e.g., X-rays) the periodic crystal planes diffract the waves, as do diffraction gratings at visible frequencies, and the spatial dependence must be explicitly incorporated into any description of the dielectric function. For many

plasmonic materials and metamaterials this distinction is important since the size of the metallic structures is often at the boundary where spatial frequency dependence is required. Diffraction and scattering may also cause depolarization which is important to take into account in ellipsometry measurements.

If ε and μ are independent of both spatial and temporal frequency, Eq. (2.3) becomes

$$k = \frac{\omega}{c}\sqrt{\varepsilon\mu} \tag{2.4}$$

Limiting ourselves for now to non-magnetic materials[1] the material permittivity $\varepsilon = 1 + \mathbf{P}/\mathbf{E}\varepsilon_0$ (also called the dielectric constant) is a measure of the macroscopic electric polarizability of a material. All materials exhibit temporal frequency dispersion and ε is a complex function of angular frequency ω such that $\varepsilon(\omega) = \varepsilon'(\omega) + i\varepsilon''(\omega)$, where the sign of the imaginary part is consistent with the convention used in physics [19]. It is assumed from this point that the frequency dependence is implicit in ε. The dielectric function is related to the complex index of refraction N, by $\varepsilon = N^2 = (n + i\kappa)^2$ where n is the refractive index and κ is the absorption coefficient. To avoid confusion between the absorption coefficient and the wave vector we will endeavour to use the dielectric function where possible. The dielectric function is also related to the optical conductivity σ by $\varepsilon = 1 + i\sigma/\varepsilon_0\omega$ [24].

If one assumes the dependence on spatial frequency is negligible then we may assign a dielectric tensor to a material. In the general case

$$\overleftrightarrow{\varepsilon} = \begin{bmatrix} \varepsilon_{xx} & \varepsilon_{xy} & \varepsilon_{xz} \\ \varepsilon_{yx} & \varepsilon_{yy} & \varepsilon_{yz} \\ \varepsilon_{zx} & \varepsilon_{zy} & \varepsilon_{zz} \end{bmatrix} \tag{2.5}$$

For the case of a surface or thin film, the tensor axes are generally defined in orthogonal Cartesian coordinates with the x and y axes parallel to the surface and the z-axis in the direction normal to the plane. If the material optical properties are orthorhombic [19], one may apply a transformation matrix by defining the Euler rotation angles to rotate the dielectric function such that the principle material axes align with the laboratory axes. Then the diagonal tensor elements reduce to ε_x, ε_y and ε_z and the off-diagonals are zero. For isotropic materials $\varepsilon_x = \varepsilon_y = \varepsilon_z$. For materials with monoclinic or triclinic optical properties, one may apply a further rotation using a transfer function to determine the angles between the principle axes [25].

2.2. Ellipsometric measurement

There are two standard techniques to determine the dielectric function of a material; reflection and transmission (R&T) measurements, and ellipsometry. R&T measures the intensity of transmitted and/or reflected light after interaction with a material. By combining the R&T data one can determine the complex permittivity. If only one of the measurements is available (e.g., the material may be opaque) then it is possible to use the Kramers–Kronig (KK) theorem to determine the dielectric function. However, there is often an associated uncertainty in the value of ε'. In contrast, ellipsometry measures the change in polarization state of light reflected from a material. The advantage of ellipsometry is the simultaneous measurement of both the amplitude ratio and phase difference of orthogonally polarized light (Fig. 1). This provides two measured parameters with which to calculate the real and imaginary parts of the dielectric function, thereby avoiding the need to resort to KK analysis. In addition, by measuring ratios of the intensities, calibration procedures are simplified.

Ellipsometry exploits the fact that polarized light, at off-normal incidence, is reflected (and transmitted) differently from a surface depending on whether its electric field is aligned parallel (p) to the plane of incidence, or perpendicular to it (s, from the German, *senkrecht*). Fig. 1 shows the case of light reflected from a surface which originally contains equal components of s- and p-polarized light (i.e., linearly polarized with electric field oriented 45 degrees from the incidence plane). The contrast in the dielectric functions at the interface causes the phase of one component to be delayed with respect

[1] For most natural materials $\mu = 1$ at frequencies higher than the microwave region [23].

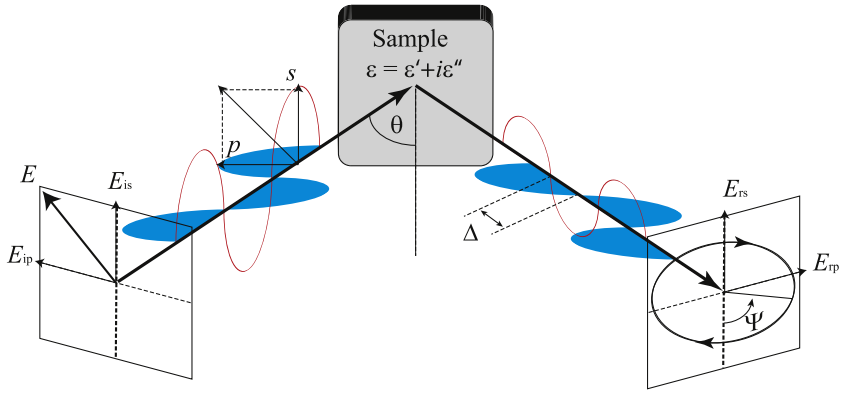

Fig. 1. Ellipsometric measurement geometry.

to the other by an amount Δ and the reflected electric field amplitudes to be dissimilar. Thus, in general, the reflected light will be elliptically polarized. While the case described above uses linearly polarized incident light, the ellipsometric principle applies to elliptically polarized incident light or even modulated incoming state-of-polarization. So long as the initial polarization state is known, the dielectric function of the sample may be deduced from a measurement of the ellipticity of the final state; hence the term ellipsometry.

2.2.1. The Stokes formalism

In the most general description the polarization state of a light beam is described by the Poincaré sphere or the Stokes formalism. The Stokes method defines parameters which are directly measureable as irradiance, I. The Stokes parameters in vector form are defined by [26]

$$S_0 = I_x + I_y \tag{2.6a}$$

$$S_1 = I_x - I_y \tag{2.6b}$$

$$S_2 = I_{+45} - I_{-45} \tag{2.6c}$$

$$S_3 = I_R - I_L \tag{2.6d}$$

where the subscripts denote polarization in the orthogonal x and y directions, at 45 degrees to x and y, and right circularly and left circularly polarized. The Stokes vector is simply

$$\mathbf{S} = \begin{bmatrix} S_0 \\ S_1 \\ S_2 \\ S_3 \end{bmatrix} \tag{2.7}$$

The 4×4 Mueller matrix represents the transformation of an incident Stokes vector $\boldsymbol{S}_i$ to its reflection from a sample surface $\boldsymbol{S}_r$.

$$\mathbf{S}_r = \begin{bmatrix} m_{11} & m_{12} & m_{13} & m_{14} \\ m_{21} & m_{22} & m_{23} & m_{24} \\ m_{31} & m_{32} & m_{33} & m_{34} \\ m_{41} & m_{42} & m_{43} & m_{44} \end{bmatrix} \mathbf{S}_i \tag{2.8}$$

A complete or partial measurement of the Mueller matrix using ellipsometric concepts is referred to as Mueller matrix ellipsometry (MME). Knowledge of the Mueller matrix provides practically all information about the interaction of polarized light with the sample. Complete measurement of all

16 elements of the matrix is therefore somewhat of a holy grail for applied ellipsometrists. The first MME measurements were performed in the late 1970s, however only recently has the hardware become generally available to perform such measurements [27].

MME is necessary if the sample depolarizes the probe beam (i.e., converts it to partially polarized or unpolarised light). There are a number of common causes of depolarization and one should always be mindful of the potential for its occurrence since it may significantly alter the results of an ellipsometric analysis. Primary causes include; large sample surface roughness causing scattering of the probe beam; thin film thickness inhomogeneity (e.g., thickness gradient); backside reflection from a weakly absorbing substrate; and variation in the incident angle of the probe beam (e.g., caused by focusing optics). Depolarisation has been used as a technique to determine the thickness gradient in thin films [28,29] and proposed as a method to determine the roughness of a surface [30]. Depolarization phenomena occur not only for heterogeneous samples. Strongly varying optical properties as a function of wavelength (strong dispersion) or incident angle can induce depolarization. Thus plasmonic resonances cause depolarization effects.

2.2.2. The Jones formalism

If the sample is non-depolarizing, a 4 × 4 Mueller matrix (with real valued elements) may alternatively be described using a 2 × 2 Jones matrix (with complex valued elements) [18]. In the Jones formalism one defines the polarization states as orthogonal electric field components, E_p and E_s. Reflection from a surface of a propagating light ray is expressed by the Jones matrix [31]

$$\begin{bmatrix} E_{rp} \\ E_{rs} \end{bmatrix} = \begin{bmatrix} r_{pp} & r_{ps} \\ r_{sp} & r_{ss} \end{bmatrix} \begin{bmatrix} E_{ip} \\ E_{is} \end{bmatrix} \tag{2.9}$$

where matrix elements are the reflection coefficients and the subscripts r and i denote the reflected and incident rays, respectively (note that the ordering of the subscripts are interchanged in some notations [21]). In isotropic materials the off-diagonal elements, r_{ps} and r_{sp} (which correspond to the reflected p-polarized light induced by incident s-polarized light, and the reflected s-polarized light induced by incident p-polarized light, respectively [19]) are zero. The diagonal elements r_{pp} and r_{ss} may then be simply written r_p and r_s. This allows one to define the ellipsometric parameters, Ψ and Δ, as the ratio of the reflection coefficients

$$\rho \equiv \frac{r_p}{r_s} \equiv \tan\Psi e^{-i\Delta} \tag{2.10}$$

The angles Ψ and Δ correspond to the amplitude ratio and the phase difference of the reflection coefficients, respectively. The parameter ρ is in practice directly measureable, however in modern rotating element ellipsometers one generally measures Fourier coefficients of the detector and converts them to the Jones matrix [32].

2.2.3. Generalized ellipsometry

If the film and/or substrate are optically anisotropic a proportion of incident p-polarised light is converted to s-polarised light (and vice versa) and the off-diagonal elements of the Jones matrix are non-zero. They must be determined using generalized ellipsometry (GE), introduced by Azzam and Bashara [33] in the early 1970s. The basic principle is to define and determine three independent normalized Jones matrix elements for fixed measurement geometry. The GE parameters Ψ_{ij} and Δ_{ij} are defined by [19]

$$\rho_{pp} \equiv \frac{r_{pp}}{r_{ss}} = \tan\Psi_{pp} e^{-i\Delta_{pp}} \tag{2.11a}$$

$$\rho_{ps} \equiv \frac{r_{ps}}{r_{ss}} = \tan\Psi_{ps} e^{-i\Delta_{ps}} \tag{2.11b}$$

$$\rho_{sp} \equiv \frac{r_{sp}}{r_{ss}} = \tan\Psi_{sp} e^{-i\Delta_{sp}} \tag{2.11c}$$

Note that r_{pp} is also used in some works to normalise the Jones matrix elements. As pointed out by Schubert, different normalizations may be appropriate for different ellipsometric configurations [34]. To measure the six independent parameters (Ψ_{pp}, Ψ_{ps}, Ψ_{sp}, Δ_{pp}, Δ_{ps}, Δ_{sp}) that define the Jones matrix requires at least three independent measurements with different angles of light polarization [18]. In practice, the system is usually over-determined by measuring a large number of polarization angles.

2.3. Parameter retrieval

Predicting reflection and transmission spectra by solving Maxwell's equations for specific geometries and permittivities is often termed the "forward problem". We are concerned with the "reverse problem"; the retrieval of the permittivities and geometries from reflection and transmission spectra. Solving the reverse problem for complicated structures using reflection spectra has been compared with trying to determine "the shape of a dragon from its footprints" [35]. Therefore we need to start with simple problems and work our way up. In the simplest case of reflection from a planar interface between two semi-infinite materials the reverse problem reduces to determining the pseudodielectric function using the Fresnel equations [22].

2.3.1. The pseudodielectric function

To describe the angle-dependent refraction and reflection of light at a sharp interface between two media with real refractive indexes, n_0 and n_1, we recall Snell's law

$$n_0 \sin\theta_0 = n_1 \sin\theta_1 \tag{2.12}$$

and the Fresnel equations

$$r_p = \frac{n_1 \cos\theta_0 - n_0 \cos\theta_1}{n_1 \cos\theta_0 + n_0 \cos\theta_1} \tag{2.13}$$

$$r_s = \frac{n_0 \cos\theta_0 - n_1 \cos\theta_1}{n_0 \cos\theta_0 + n_1 \cos\theta_1} \tag{2.14}$$

where θ is the angle the wave vector makes with the surface normal (Fig. 1). Whilst Eqs. (2.12), (2.13), and (2.14) are written for real valued n, they are valid for complex values, $N = n + i\kappa$. Recalling $N^2 = \varepsilon$, we can combine Eqs. (2.10) with (2.12), (2.13) and (2.14) for a relation connecting the dielectric functions of the two media

$$\langle\varepsilon\rangle = \varepsilon_0 \sin^2\theta_0 + \frac{(1-\rho)^2(\sin^2\theta_0)(\tan^2\theta_0)}{(1+\rho)^2} \tag{2.15}$$

where $\langle\varepsilon\rangle$ is termed the pseudodielectric function.[2] In the case that surface layers can be neglected $\langle\varepsilon\rangle = \varepsilon_1$. Thus assuming the ambient dielectric function is known ($\varepsilon_0 \approx 1$ for air) then the material dielectric function may be determined from the incident angle θ_0 and the reflectance ratio ρ. Since ellipsometry measures two values the retrieval procedure can unambiguously determine both the real and imaginary parts of the dielectric function.

2.3.2. Thin films

The pseudodielectric function only works for the case where there is no thin film or overlayer on the surface. If light is able to penetrate the film and reflect from the film/substrate interface the effects of multiple reflections in the film must be accounted for. The application of ellipsometry to plasmonics deals with the optical properties of thin films, the basics of which are well presented by Abelés [36]. The Abelés method to determine the dielectric properties of thin films and stratified media treats each layer as a 2×2 matrix [37]. A final transfer matrix is then determined from the product of all the layers [32]. The Abelés method has the advantage that it can be used for anisotropic films in certain cases, and can be easily extended to the 4×4 Berreman method for general anisotropic cases. In

[2] Note that here ε_0 is the ambient dielectric function, not the vacuum permittivity.

the special case that there is only a single isotropic thin film of thickness d on a substrate, the Abelés method reduces to the well known Airy formulas

$$r_{012p} = \frac{r_{01p} + r_{12p}\exp(\mathrm{i}2\beta)}{1 + r_{01p}r_{12p}\exp(\mathrm{i}2\beta)} \tag{2.16a}$$

$$r_{012s} = \frac{r_{01s} + r_{12s}\exp(\mathrm{i}2\beta)}{1 + r_{01s}r_{12s}\exp(\mathrm{i}2\beta)} \tag{2.16b}$$

where

$$\beta = \frac{2\pi d N_1 \cos\theta_1}{\lambda} \tag{2.17}$$

and the subscripts 0, 1 and 2, denote the ambient, film and substrate respectively. Multilayer systems may be analysed in a similar way by extending this procedure although it is rather cumbersome and the Abelés method is recommended.

The film thickness is often unknown. If the dielectric functions of all layers are known then the film thickness may be determined with great accuracy. However care must be taken since the thin film dielectric function often differs markedly from the bulk. If only the substrate and ambient dielectric functions are known then the three unknowns (ε_1', ε_1'', d) cannot be uniquely determined from the two ellipsometric parameters. If ε_1'' is very small (e.g., transparent glass or polymer) then the problem may be approximated to two unknowns. However for metal films ε_1'' is significant and other methods are required. One method is to use a prominent optical feature in the substrate. If d is incorrect then this feature will appear in the film dielectric function. Thus, d may be iteratively adjusted to remove the feature and obtain the correct thickness and dielectric functions. This method has been termed the "Arwin-Aspnes" method if the feature is a semiconductor transition [38] or the "interference" method if the feature arises from an interference fringe from a thick transparent film on the substrate [39]. Characterization of thin absorbing films with ellipsometry has been reviewed by Hilfiker et al. [40] .

2.3.3. Anisotropic thin films

The Fresnel approach to determine anisotropic dielectric tensors is quite demanding and the use of the 4×4 matrix method is generally employed. The method is based on the Berreman transfer matrix method [41] and was established by Schubert in its currently used form [42,43]. Briefly, one defines an incident matrix to project the electric fields of the transmitted wave onto the rear surface of the film. Those fields are then projected to the top surface by a 4×4 partial transfer matrix which is defined using the material dielectric functions. Finally an exit matrix projects the fields into the incident and reflected waves. Further partial transfer matrices may be introduced to account for multiple layers. The incident, exit and partial transfer matrices are then multiplied to give a final transfer matrix. The elements of the Jones matrix are determined from algebraic ratios of the transfer matrix elements and compared with the measured values.

2.3.4. Fitting procedure in ellipsometry

By constructing an optical slab model of parallel layers for the substrate and any overlayers the parameters defining the layers, such as the thickness and optical constants, may be determined by fitting to measured data. In the simplest case of a flat bulk absorbing material, the problem reduces to determining the optical constants using Eq. (2.15). In that case the number of unknowns is equal to the number of measured parameters and the system is uniquely determined. A similar case occurs for a thin film if the thickness is known, as described above. However using spectroscopic data we may also be interested in determining the parameters which define the optical constants, such as the electron density or mean-free-path using the models described in Section 3. In that case we can define a number of fitting parameters in the model and – using an error fitting function – minimize the error between the model and the experimental data using a linear regression analysis, such as the Levenberg–Marquardt method. The fitting procedure is described in greater detail in Ref. [19].

3. Optical models of metals

The features of the dielectric function in the visible region arise from the response of bound and unbound charges to the electric and magnetic fields of light. The optical properties of metals stem predominantly from unbound conduction electrons, which give rise to the plasmons which we are interested in, although the bound electrons have a significant influence. The Lorentzian model is the general starting equation for the resonant behaviour of bound electrons in an electric field. For transparent dielectrics, the Sellmeier model is a special case Lorentzian where the absorption is zero. The Drude model of metals is a special case Lorentzian where the resonance frequency is zero.

3.1. The Lorentz model

The Lorentz model describes the motion of an electron bound to a positive ion core in an electric field. We assume that the motion of the ion core is negligible and that there is a linear restoring force on the electron. The electron with mass, m_e and charge, $-e$, in an external electric field, $\mathbf{E} = \mathbf{E}_0 \exp(-\mathrm{i}\omega t)$, has the equation of motion

$$m_e \frac{\mathrm{d}^2 x}{\mathrm{d}t^2} = -m_e \Gamma \frac{\mathrm{d}x}{\mathrm{d}t} - m_e \omega_0^2 x - e\mathbf{E}_0 \exp(-\mathrm{i}\omega t) \tag{3.1}$$

The first term on the right hand side accounts for damping of the oscillation due to scattering from defects and impurities, where Γ is the damping constant. The second term accounts for the restoring force where ω_0 is the resonance frequency of the oscillation. The final term is the electrostatic force from the externally applied field.

For a material where the number of electrons per unit volume is N_e, the polarization becomes $\mathbf{P} = -eN_e x(t)$. Combining Eqs. (2.1) and (3.1) and rearranging gives us

$$\varepsilon(\omega) = 1 + \frac{e^2 N_e}{\varepsilon_0 m_e} \frac{1}{\omega_o^2 - \omega^2 - \mathrm{i}\Gamma\omega} \tag{3.2}$$

This is the expression for a Lorentz oscillator. It is particularly effective for modelling chemical bonds at infra-red frequencies. If the material is a non-absorbing dielectric, such as a transparent glass or polymer, we may set Γ to zero, giving us the Sellmeier model. The commonly used Cauchy model is an approximation of the Sellmeier model in terms of the real refractive index, n.

3.2. The Drude model

Conduction electrons in a free-electron metal (such as the noble metals) are essentially unbound. The Drude–Sommerfeld model assumes that the conduction band electrons act in phase in response to an applied electric field. Since there is essentially no restoring force on the electrons, the centre frequency of Eq. (3.1) is zero, resulting in the Drude equation[3]

$$\varepsilon(\omega) = 1 - \frac{\omega_p^2}{\omega^2 + \mathrm{i}\Gamma\omega} = 1 - \frac{\omega_p^2}{\omega^2 + \Gamma^2} + \mathrm{i}\frac{\omega_p^2 \Gamma}{\omega\left(\omega^2 + \Gamma^2\right)} \tag{3.3}$$

where ω_p is the Drude plasma frequency defined by

$$\omega_p = \sqrt{\frac{e^2 N_e}{\varepsilon_0 m_e}} \tag{3.4}$$

The mass of the electron may be replaced by an effective mass, m_0, to describe the coupling to the ion core. This is especially important in semiconductors. The collective motion is damped by scattering from surfaces, defects and grain boundaries in the metallic crystal. The damping constant, Γ, is related to the electron mean free path, l, by

[3] Note that the sign in the denominator is reversed to denote losses.

$$\Gamma = \frac{v_f}{l} = \frac{1}{\tau} \tag{3.5}$$

where v_f is the Fermi velocity and τ is the collision frequency. Thus the DC conductivity σ_0 of a metal may be determined from the Drude model via the relation

$$\sigma_0 = \frac{e^2 N_e}{m_e}\tau = \frac{\omega_p^2 \varepsilon_0}{\Gamma} \tag{3.6}$$

3.3. Interband transitions

In real metals the bound electrons contribute to the dielectric function, especially in the UV region where interband transitions are excited. In the noble metals – which are the materials of choice for plasmonics – the lowest energy interband transitions occur at $\hbar\omega$ = 2.1, 3.8 and 2.4 eV for Cu, Ag and Au respectively [44]. These correspond to transitions from the 3*d*-4*s*, 4*d*-5*s* and 5*d*-6*s* bands, respectively. For energies below the transition edge there is negligible contribution to the imaginary part ε''. The contribution to the real part ε' may be approximated by a constant offset ε_∞. Eq. (3.3) thus becomes

$$\varepsilon(\omega) = \varepsilon_\infty - \frac{\omega_p^2}{\omega^2 + \mathrm{i}\Gamma\omega} \tag{3.7}$$

The accuracy of this model decreases as the transition energy is approached. The interband transition may be explicitly modelled with multiple Lorentz-oscillators [45] but this does not take into account the actual band-gap. The Tauc–Lorentz (TL) model, on the other hand, explicitly incorporates the band-gap. The model described by Jellison and Modine [46] combines the Lorentzian equation (Eq. (3.1)) with an expression for ε'' developed by Tauc et al. [47] and expanded by Forouhi and Bloomer [48]. It describes interband mechanisms with an optical band gap $\hbar\omega_g$. The final expression is

$$\varepsilon''(\omega) = \frac{A\omega_0\Gamma(\omega-\omega_g)^2}{(\omega^2-\omega_0^2)^2 + \Gamma^2\omega^2}\cdot\frac{1}{\omega} \tag{3.8}$$

for frequencies above the gap and $\varepsilon''(\omega)$ = 0 for frequencies equal to or below the gap. In Eq. (3.8) the fitting parameters *A*, ω_0, Γ and ω_g are the amplitude, centre frequency, broadening and band gap frequency, respectively. ε' is obtained by Kramers–Kronig integration. Away from the band edge Lorentzian oscillations are useful to account for further structure in the dielectric function. Note that Eq. (3.8) was originally derived for amorphous materials and its applicability to a crystalline material is debatable. However it was successfully applied for crystalline materials such as TCOs [49] and high-κ dielectrics [50] and an equivalent formula also gives a reasonable representation of the interband transitions in Au [51].

3.4. Dielectric functions of the noble metals

The noble metals (or coinage metals) are of great practical interest in plasmonics for two reasons. Firstly, they are comparatively inert. In particular, gold is widely used in biomedical applications. Secondly, the noble metals have comparatively low damping constants Γ, especially silver which has a small Γ across the entire visible spectrum. Thus the plasmon resonances are quite narrow and losses acceptable. Fig. 2 shows the experimental data of Palik for silver [52] with fits of the Drude (Eq. (3.7)) and Tauc–Lorentz (Eq. (3.8)) expressions in the range $\hbar\omega = 1$—6 eV. The parameter ε_∞ (fit value = 1.64 eV) is included to account for interband transitions at higher energies. At energies below the band edge (3.7 eV) the TL is zero for the imaginary part and approaches a constant value for the real part. Close to the band edge the model underestimates the imaginary part.

In the majority of works in the literature concerning the optical properties of gold, silver and copper, the experimentally determined dielectric functions of Johnson and Christy [53] in the energy range $\hbar\omega = 0.5$—6.5 eV are utilized as input parameters for theoretical predictions or as references

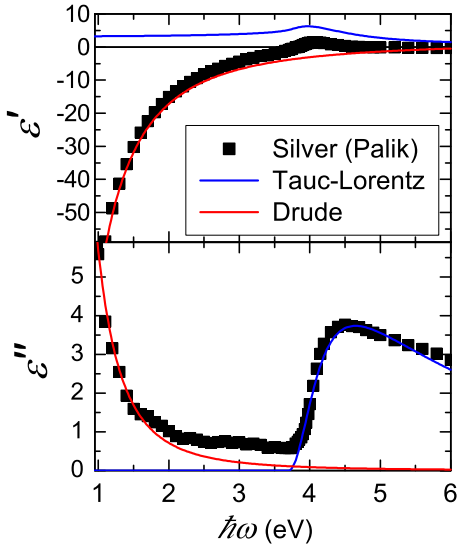

Fig. 2. Experimental data for the dielectric function of silver from Ref. [52] fit with the Drude (Eq. (3.7)) and Tauc–Lorentz (Eq. (3.8)) expressions.

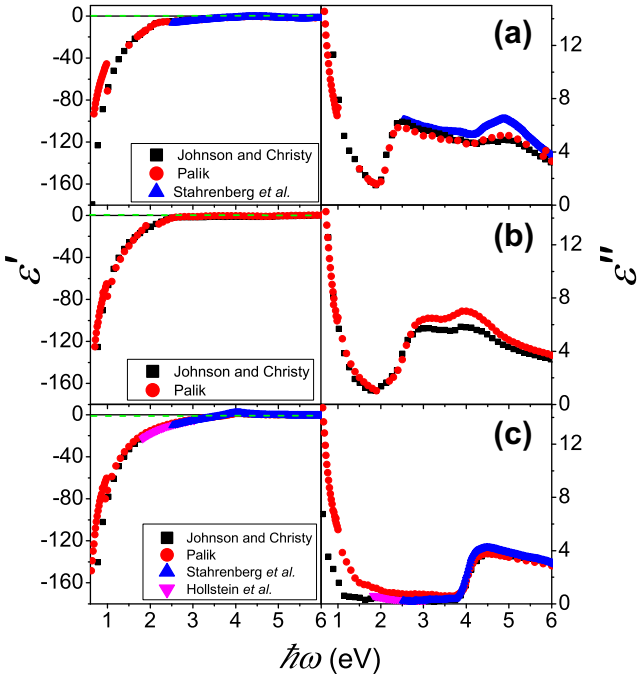

Fig. 3. Dielectric functions of (a) copper, (b) gold and (c) silver from experimental data of Palik [52] Johnson and Christy [53], Hollstein et al. [56] and Stahrenberg et al. [57].

Table 3.1
Drude model parameters in units of eV for the dielectric functions of the noble metals using the data of Johnson and Christy [53].

	ε_∞	$\hbar\omega_p$	$\hbar\Gamma$	E_g
Cu	7.96	8.88	0.1015	2.08
Ag	4.10	9.18	0.0207	3.86
Au	10.30	9.05	0.0778	2.38

for experimental measurements. The real and imaginary parts are shown in Fig. 3. The data shows a number of discontinuities, especially around 1 eV. Palik's Handbook of Optical Constants gives slightly different values [52] and for silver in the Drude region the data is more consistent, although there is a discontinuity around 1 eV. Alternative dielectric functions for 12 metals (including the noble metals) were published by Ordal et al. in the infrared region [54,55] and Holstein et al. for Cu and Ag in the intermediate region between pure Drude and interband transitions (1.8–3 eV) [56]. More recently, measurements in the range from 2.5 to 9 eV were presented by Stahrenberg et al. for Cu and Ag under UHV conditions [57] (available on request [58]). Parameterized dielectric functions of 11 metals were published by Rakic et al. with the interband transitions fit using multiple Lorentzians [59]. The data of a number of the above references are plotted together in Fig. 3 for copper, gold and silver. Note the difference in the onset of the interband transitions in the different materials.

In Table 3.1, we list model parameters fit using the Drude model of Eq. (3.7) to the data of Johnson and Christy [53] from 0.6 eV to the onset of interband transitions, $E_g = \hbar\omega_g$ [60]. This provides an accurate description of the dielectric function in the energy range from virtually DC to E_g. Note that the intraband parameters ω_p and Γ are quite similar for the three metals, whereas the interband parameters E_g and ε_∞ differ markedly. The value of E_g is instrumental in determining the colour of the metal; photons of energy less than E_g will be strongly reflected.

3.5. Materials other than the noble metals

Whilst the noble metals dominate the literature on plasmonics there has been a recent push to investigate alternative materials [61]. This is primarily aimed at finding low-loss materials and a desire to move to other regions of the EM spectrum. Sodium and potassium also have much lower losses than silver however they are highly reactive in air and therefore impractical. Their plasmonic properties are well discussed in [60]. Aluminum, gallium, platinum and palladium have also been demonstrated as plasmonic materials although their losses are higher than the noble metals. Aluminium has a plasma frequency in the UV and an interband transition at 1.5 eV. The surface oxidation of aluminium can be used to advantage in practical applications, however it complicates modelling [62,63]. Gallium also has a plasmon frequency in the UV and it is stable upon exposure to air. Gallium nanoparticles have the interesting property of being a liquid in the temperature range from −80 to 600 °C. Wu et al. [64–66] have performed a number of spectroscopic ellipsometric studies on the plasmon resonances of Ga nanoparticles and their relationship to the deposition conditions, substrate material and Raman enhancement. Gallium/aluminium composite has also been investigated as a potential material for optical modulation of plasmonics resonances [67]. Palladium and platinum are also interesting materials, especially in regards to hydrogen storage and catalysis [68,69]. The particle plasmon resonances (discussed below) of these and other metals are presented in Ref. [60]. Whilst the problem of losses will not easily be overcome by changing the conductive material, other work has focused on reducing the apparent losses by embedding the plasmonic elements in a gain medium [70].

Looking to unconventional materials, large band-gap doped oxides, also called transparent conductive oxides (TCOs), such as zinc oxide, both aluminium and gallium doped, and tin doped indium oxide (ITO), have plasma frequencies in the infrared [71]. The electron density and therefore the plasma frequency can be tuned by adjusting the doping in these materials. This creates a novel way to tune the plasmon resonance frequency. A number of recent studies on the plasmon resonances in ITO have been presented by Franzen et al. [72–76], discussed further in Section 4.2. The imaginary part of the dielectric function of ITO from ref [49] is shown in Fig. 4. The interband transitions occur at ener-

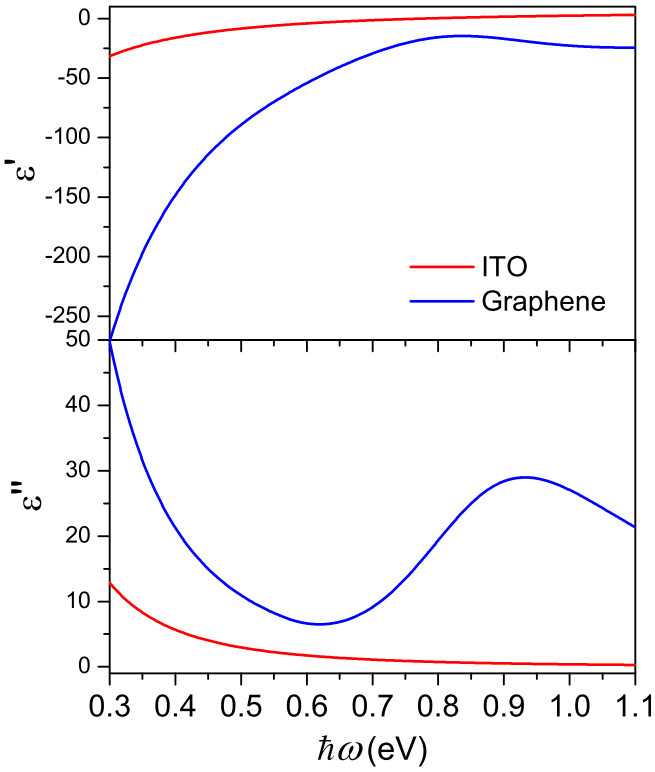

Fig. 4. Imaginary part of the dielectric functions of graphene (generated from theory in [79]) and ITO (fitted model from measured data in [71]).

gies above 3.5 eV (not shown). Graphene has been trumpeted as a wonder material due to its extremely high mobility (and therefore low losses) [77] and has been theoretically proposed in plasmonic applications [78]. One interesting aspect of graphene is the ability to tune not only the plasma frequency but also the onset of the interband transition by shifting the Fermi level by applying a gate bias. Fig. 4 shows a theoretical prediction of the imaginary part of the dielectric function of pristine graphene with a Fermi energy of 0.6 eV, with the thermally broadened interband transition at 1.2 eV (twice the Fermi energy) [79]. Note the similarity in shape to the silver dielectric function, with the energies shifted into the IR.

3.6. Volume plasmons

In a pure Drude metal, Eq. (3.3) indicates that if Γ is very small then $\varepsilon(\omega_p) \rightarrow 0$. Collective longitudinal optical (LO) modes can propagate in a material when $\varepsilon = 0$ and in the visible range this is termed the volume plasmon frequency or the "bulk" plasmon frequency. Excitation of LO modes was initially performed using electron energy loss spectroscopy (EELS) through thin metal films by Ferrell [80] and explained theoretically by Ritchie [81]. McAlister and Stern [82] showed that in very thin films, p-polarized light incident at an oblique angle can excite resonances normal to the film plane which appear as absorption bands in reflection and transmission measurements. In a thin film of conductor these modes are plasmon resonances termed Ferrell modes. In ionic dielectrics analogous phonon modes may be excited which are known as Berreman modes [83].

To describe the effect we consider a thin slab of pure Drude material. Displacement of a region of the electronic cloud by a distance *x*, results in a surface charge density *Nex*, where *N* is the electron

density. Thus an electric field is established inside the slab, $E = Nex/\varepsilon_0$ resulting in a restoring force on the displaced electrons,

$$\mathbf{F} = -e\mathbf{E} = -\frac{Ne^2x}{\varepsilon_0} = m\frac{\mathrm{d}^2x}{\mathrm{d}t^2} \tag{3.9}$$

or

$$\frac{\mathrm{d}^2x}{\mathrm{d}t^2} = -\frac{Ne^2x}{m\varepsilon_0} = -\omega_p^2x \tag{3.10}$$

The electrons thus oscillate at a natural frequency equal to the plasma frequency, ω_p.

For a real material, the volume plasmon is not found at ω_p but is red shifted as a result of the interband transitions. Using Eq. (3.7) and calculating the frequency at which the real part is zero gives the screened plasmon frequency ω_ps

$$\omega_\mathrm{ps}^2 = \frac{\omega_p^2}{\varepsilon_\infty} - \Gamma^2 \tag{3.11}$$

Thus interband transitions have a strong influence on the observed values of the bulk plasmon in the noble metals. For both silver and gold, Eq. (3.3) predicts the bulk plasmon energy at around 9 eV, as observed in Table 3.1 for $\hbar\omega_p$. Using Eq. (3.11) gives a $\hbar\omega_p$'s of 4.5 and 2.8 eV for silver and gold, respectively. However experimental values are around 3.8 and 6 eV, respectively. The discrepancy is due to the poor representation of Eq. (3.7) above E_g. Note that in Eq. (3.10) there is no dependence on the film thickness. In optical experiments the thickness must be less than the skin depth and phase retardation becomes important when the thickness is not significantly less than the wavelength.

In gold ε'' is comparatively large at ω_ps and the LO mode is strongly damped and thus rarely observed in optical experiments. The LO mode is observed in oblique angle p-polarized reflection from thin silver films in the UV [84] and films of transparent conducting oxides at infrared frequencies [75]. To demonstrate the effect on ellipsometric measurements, Fig. 5 shows calculated ellipsometric angles and s- and p-polarized transmission and reflection at an incident angle of 75° for a 20 nm thick free-standing silver film. We use the bulk dielectric function from [52], fit using a parameterized model as in Fig. 2. s-Polarised reflection and transmission is closely related to ε'', whereas *p*-polarised reflection and transmission shows a strong feature close to ω_ps, which is also observed in the ellipsometric angles.

4. Surface plasmon polaritons

The bulk plasmons described above are radiative modes that may be excited by fast electrons or oblique incidence photons. Once excited they will oscillate until they decay either by spontaneous photon emission or collisional damping. Alternatively a plasmon may couple to a photon and propagate with the same wave vector. If the photon is subsequently decoupled then the plasmon is extinguished. A coupled photon and plasmon is termed a *plasmon polariton* [85]. Propagation of EM waves is forbidden in materials where ε' is negative, such as metals below the plasma frequency. An EM wave may however propagate as a surface bound wave or surface electromagnetic wave (SEW) and when coupled to a photon it is called a *surface plasmon polariton* (SPP). SPPs are reviewed extensively in a number of texts [86,87].

The SPP phenomenon may be exploited for biosensing and is commonly referred to as the surface plasmon resonance (SPR) technique [88]. The irradiance of internally reflected p-polarized light from a thin gold layer on glass strongly depends on the adsorbed mass of biomolecules on the gold surface. A minimum (the SPR dip) in the reflectance curve is then obtained when the polarization, angle of incidence, gold layer thickness and wavelength are optimized to excite an SPP. In principle all energy from the EM wave can be coupled over to the plasmon wave at resonance. The angular position of the dip becomes very sensitive to the refractive index of the medium close to the gold layer (within the evanescent field depth). If biomolecules adsorb onto the gold layer they can therefore easily be detected and quantified. In most sensor applications, the angular position of the SPR-dip is measured whereby

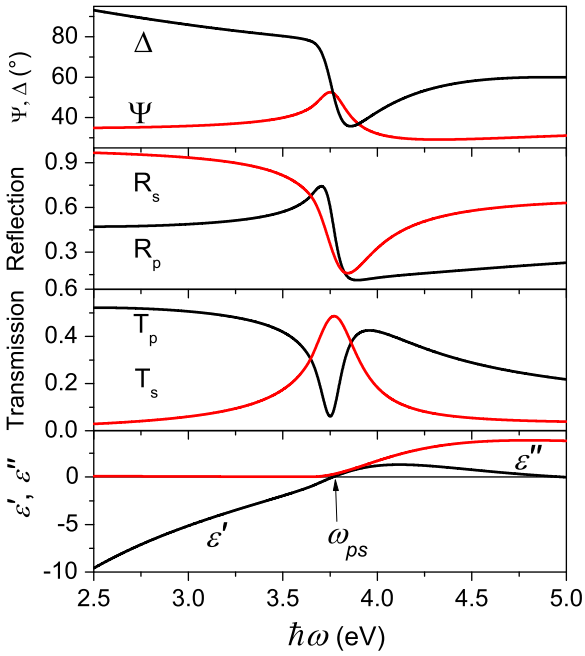

Fig. 5. The ellipsometric angles, Ψ and Δ, and the reflection and transmission of s- and p-polarized light from a 20 nm free-standing silver film. At the screened plasma frequency, ω_{ps}, the real part of the dielectric function is zero and an LO plasmon is excited in the film.

irradiance measurements are performed and thus the amplitude information of the reflected light is monitored. However, also the phase difference between the p- and s-polarized waves carries information about the SPP excitation. This phase difference is the ellipsometric parameter Δ and it has been shown that monitoring Δ can give even higher sensitivity than monitoring irradiance [89].

4.1. The dispersion relation of a SPP

The study of SPP excitation and propagation is analogous to the study of related quasiparticle polaritons in solids, such as phonons, magnons and excitons [90]. The full derivation of the surface polariton dispersion relation is presented in a number of texts (e.g., [86,90]) and is obtained by solving Maxwell's equations with appropriate boundary conditions, which for surface polaritons is defined by the interface between two semi-infinite media coupled by continuity at the boundary. Since this is analogous to the boundary conditions for the Fresnel reflection coefficients we may use them as the starting point and look for a solution for a wave propagating along the surface.

Due to the electric dipoles created by the redistribution of charges in a plasmonic wave (shown schematically in Fig. 6), an electromagnetic wave propagating in the surface plane must have a component of electric field perpendicular to the surface. Since the electric field of s-polarized light is always parallel to the surface (a transverse electric or TE wave) we conclude that only the component of p-polarized light with electric field perpendicular to the surface (a transverse magnetic or TM wave) can couple to a surface plasmon mode on a flat metal surface. At resonance $r_p = 0$ and the p-polarized Fresnel reflection coefficient at a single interface between a metal and ambient becomes [20]

$$\frac{k_{z,m}}{\varepsilon_m} + \frac{k_{z,a}}{\varepsilon_a} = 0 \tag{4.1}$$

where k_z is the wave vector in the z direction (perpendicular to the interface), and the subscripts m and a denote the metal and ambient, respectively. One case in which (4.1) is fulfilled is if the signs

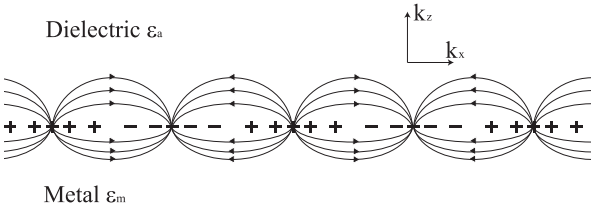

Fig. 6. Schematic of the charge distribution and electric fields of a surface plasmon polariton at the boundary between an insulator and a good conductor.

of the dielectric functions are opposite. This may be achieved when $\varepsilon'_m < 0$ (i.e., a metal below the plasma frequency) and $\varepsilon_a > 0$ (a dielectric). The field associated with the SPP has its maximum at the interface and decreases exponentially (evanescent fields) into both media with normal components of wave vectors being purely imaginary. The source of the field is a charge oscillation in the metal surface (Fig. 6). Combining (4.1) with the wave equation for a transverse wave (Eq. (2.4)) gives the dispersion relation for a SPP propagating along the interface with the x-component of the SP wave vector k_{SP}^{∞}

$$k_{SP}^{\infty} = \frac{\omega}{c}\sqrt{\frac{\varepsilon_a \varepsilon_m}{\varepsilon_a + \varepsilon_m}} = k_{SP}^{\infty'} + \mathrm{i}\Gamma^{\infty} \tag{4.2}$$

where the superscript ∞ indicates a semi-infinite geometry, and $k_{SP}^{\infty'}$ and Γ^{∞} are the real and imaginary part of k_{SP}^{∞}. We are here only concerned with surface-bound waves and normal components of the SP wave vectors ideally should be purely imaginary, otherwise a wave propagating in the z-direction would exist.

Fig. 7 shows a plot of Eq. (4.2) at the interface between a Drude metal (Eq. (3.3)) with negligible damping ($\Gamma = 0$) and vacuum ($\varepsilon_a = 1$). Below the plasma frequency, ω_p, in the limit of very small k (the retarded region) the dispersion curve approaches the light line, $\omega = ck$, whereas for large k values (the non-retarded region) the graph reaches an asymptotic value given by the solution to

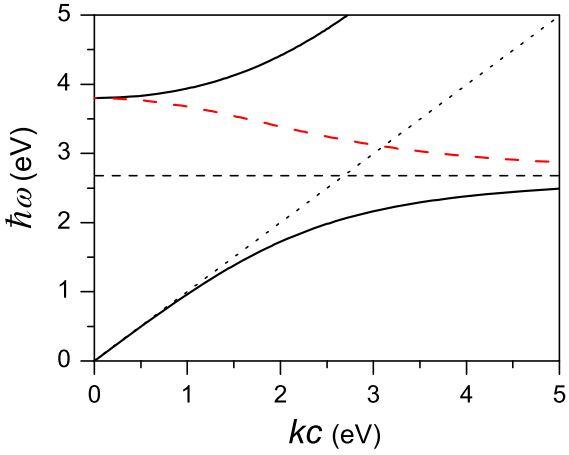

Fig. 7. The real (black solid line) and imaginary (red dash line) parts of the surface polariton dispersion, $\hbar\omega$ vs kc, Eq. (4.2), at the interface between vacuum ($\varepsilon_a = 1$) and a Drude metal (Eq. (3.3)) with $\hbar\omega_p = 3.8$ eV and negligible damping ($\Gamma = 0$). The lower branch is bounded by the light line $\hbar\omega = kc$ (dotted line) and the surface plasmon frequency, $\omega_{sp} = \omega_p/\sqrt{2}$, (dashed line). ε_m□ is positive above ω_p and light can propagate in the material (upper branch). (For interpretation of the references to colour in this figure legend, the reader is referred to the web version of this article.)

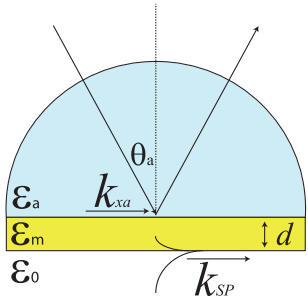

Fig. 8. The Kretschmann geometry for excitation of SPP by light through a hemispherical prism. The light with wave vector in the x-direction of k_{xa} is incident on a thin gold film of thickness d. By tunneling through the film the photons can excite a SPP at the metal–air (or metal/liquid) interface when the wave vector matches the SP wave vector, k_{SP}.

$$\varepsilon_a + \varepsilon_m = 0 \tag{4.3}$$

which for a Drude metal of Eq. (3.7) is the surface plasmon frequency, ω_{sp}, at a metal/dielectric interface

$$\omega_{sp}^2 = \frac{\omega_p^2}{\varepsilon_\infty + \varepsilon_a} \tag{4.4}$$

For a pure Drude material ($\varepsilon_\infty = 1$) in vacuum ($\varepsilon_a = 1$), Eq. (4.4) reduces to the standard expression for the surface plasmon frequency $\omega_{sp} = \omega_p/\sqrt{2}$. Above ω_p the metal is transparent and light radiates into the material, represented by the dispersion line in the upper left. Thus we have two modes; a bound SPP below ω_{sp} and a radiative mode above ω_p. Between ω_{sp} and ω_p there is a region where propagation cannot occur since the propagation constant is imaginary (red dashed line in Fig. 7). However this is only the case if one assumes a perfect conductor. In real metals the damping is significant and the dielectric function, and therefore also the propagation constant, is complex valued. Propagation in the region between ω_{sp} and ω_p is thus allowed, albeit in a *quasibound*, or so called 'leaky' mode. The bound SPPs are limited to a maximum finite wave vector at the surface plasmon frequency.

4.2. Excitation of a surface plasmon-polariton

In a standard reflection arrangement we have a beam incident at an angle θ_a. The x-component of the wave vector for the light is

$$k_{xa}^{\text{light}} = \frac{\omega}{c}\sqrt{\varepsilon_a}\sin\theta_a \tag{4.5}$$

However, for no angle of incidence we can find a match so that k_{SP}^{∞} becomes equal to k_{xa}^{light}. There are a number of methods to circumvent this problem and excite SPPs, including charged particle impacts and grating coupling. Another solution would be to come in with the light through the metal, which is impossible in the semi-infinite case due to the absorption of the metal. However if the metal is an ultrathin film then the fields can tunnel through to the metal/air interface and excite a SPP there. The Kretschmann method is based on illuminating the metal/dielectric interface through a glass prism [91]. At angles greater than the critical angle the light will be totally internally reflected inside the prism (Fig. 8) with a component in the plane of the interface. Although it is not possible to achieve momentum matching and excite an SPP at the glass/metal interface, a SPP may be excited at the metal/air (or metal/liquid) interface.

Notice that in the prism method, ε_a in (4.5) is the glass dielectric function and thus a larger k_{xa}^{light} compared to if air is used as ambient can be obtained and used to match k_{SP}^{∞}. However, for a thin metal film, the SP conditions will change compared to for a semi-infinite metal and due to the presence of the prism, a perturbation term Δk_{SP} will be added to k_{SP}^{∞} and we obtain a modified wave vector now called k_{SP} according to

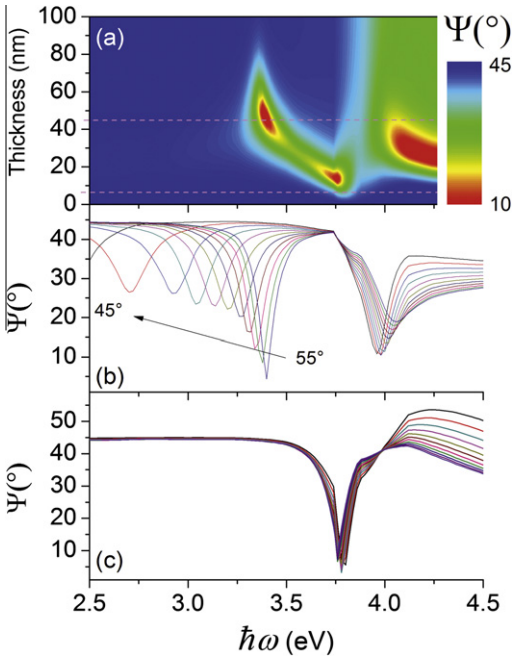

Fig. 9. The top panel (a) shows the ellipsometric angle Ψ as a function of silver film thickness and photon energy for an AOI of 55°. The bottom panels show AOI-dependent data at thicknesses of (b) 45 nm and (c) 12 nm (i.e., sections through the white dashed lines in (a)). The sharp absorption near 3.8 eV is the Ferrell mode volume plasmon resonance whereas the AOI-dependent absorption below 3.3 eV is the SPP-mode. The absorption above 3.8 eV is due to interband transitions.

$$k_{\mathrm{SP}} = k_{\mathrm{SP}}^{\infty} + \Delta k_{\mathrm{SP}} = \frac{\omega}{c}\sqrt{\frac{\varepsilon_a \varepsilon_m}{\varepsilon_a + \varepsilon_m}} + \Delta k_{\mathrm{SP}} = k_{\mathrm{SP}}^{\infty'} + \Delta k'_{\mathrm{SP}} + \mathrm{i}\left(\Gamma^{\infty} + \Gamma^{\mathrm{rad}}\right) \tag{4.6}$$

where the perturbation $\Delta k_{\mathrm{sp}} = \Delta k'_{\mathrm{sp}} + \mathrm{i}\Gamma^{\mathrm{rad}}$ is a correction that takes into account the fact that the SPPs are inherently leaky and lose energy via radiation into the prism. The perturbation term depends on the metal layer thickness and can thus be controlled. For a very large thickness, Δk_{SP} goes to zero. The excitation of the SP wave is thus obtained when

$$k_{xa}^{\mathrm{light}} = k_{\mathrm{SP}} \tag{4.7}$$

The detailed derivation of Δk_{SP} for a double interface is presented in [90].

Rhodes et al. performed an interesting study of the angular and film thickness dependence of the SPP excitation in indium tin oxide (ITO) films [73] using the Kretschmann method. The experimental results were well matched by theory using the Airy formulas (Eq. (2.16)) with glass as the ambient, vacuum as the substrate and the film modelled by the Drude equation (Eq. (3.7)). A similar theoretical demonstration is also presented for the phonon-dependent Berreman mode in the infrared by Röseler [92]. In Fig. 9 an analogous simulation is presented. Here the film dielectric function is represented by the silver data from ref [53]. The upper plot, Fig. 9(a), shows a contour plot of Ψ as a function of photon energy and silver film thickness at an angle of incidence of 55°. When the thickness reaches a few nanometres a LO bulk plasmon resonance (Ferrell mode) is observed close to the plasma energy of silver, $\hbar\omega_{\mathrm{p}} = 3.8$ eV. The bottom plot, Fig. 9(c), shows a slice through Fig. 9(a) at a thickness of 12 nm, with the angle of incidence (AOI) varied from 45° to 55°. The Ferrell mode is observed to show very little dependence on the AOI. As the film thickness is increased the Ferrell mode shifts due to retardation effects and dies out, whereas as the critical matching thickness is approached (around 45 nm) an angle-dependent absorption dip appears; the SPP mode. A slice through Fig. 9(a) at 45 nm is shown in

Fig. 9(b) with AOI from 45° to 55°, demonstrating the high angular-dependence of the SPP mode. The absorption above 3.8 eV is due to the interband transition. Note that gold has a relatively high absorption at the plasma frequency and the Ferrell mode is not observed.

4.3. SPP resonances in ellipsometric modes

Abelés [93] showed that ellipsometric monitoring of surface electromagnetic waves is very sensitive for superficial films. Experimentally a considerable enhancement in sensitivity can be obtained if ellipsometry is performed in a Kretschmann configuration. For adsorption of a protein monolayer on gold, changes in the ellipsometric parameter Δ of 90° or more are observed [94] compared to a few degrees in ordinary external mode ellipsometry [95]. After Abelés work the technique was not significantly explored until the 1990s and is now gaining interest again. The methodology has been called surface plasmon resonance enhanced ellipsometry [96], differential surface plasmon ellipsometry [97] and also total internal reflection ellipsometry (TIRE) [98]. TIRE shows several similarities to SPR techniques for sensor applications. A major difference is, however, that in SPR normally only the intensity information for reflection of p-polarized light is utilized, whereas ellipsometry in addition utilizes the s-polarization. Ellipsometry is thus more complex but has two major advantages over SPR techniques: (1) the s-polarization provides a reference for the overall irradiance transmittance and (2) not only the amplitude (irradiance) information in the reflected beam is utilized but also phase information in terms of Δ. A similar approach has earlier been proposed by Kabashin et al. [99] who suggested to enhance the resolution of SPR-based bio- and chemical sensors by using phase-polarization contrast. Earlier Nelson et al. suggested phase detection by using an SPR heterodyne phase detection sensing configuration [100] and also demonstrated that phase detection in SPR has at least five times better resolution compared to angle of incidence or wavelength detection. Nabok et al. compared TIRE with SPR by modelling of the response of TIRE to changes in the thickness and refractive index of the dielectric coating on gold, concluding a 10-fold enhancement when compared to standard SPR sensing [101].

It should be noticed that no new physics is introduced as the phenomena are fully included in the Fresnel formalism and are readily modeled in multilayer systems using e.g., scattering matrix formalisms [102]. However, such a treatment does not provide detailed insight in the physics and dependence on system parameters. To study the reflection of light at an SP we need an expression for r_p. The reflection of the s-component is of minor interest as it has no x-component and cannot couple to a SP. In the special situation with film properties and instrumental parameters selected so that an SP resonance is excited, a series of approximations can be performed on Eq. (2.16a) to derive a simplified expression for r_p near resonance. Following the derivation by Raether [86] gives

$$r_p = r_{01p}\frac{k_{xa}^{\text{light}} - (k_{\text{SP}}^{\infty'} + \Delta k'_{\text{SP}}) - \mathrm{i}(\Gamma^{\infty} - \Gamma^{\text{rad}})}{k_{xa}^{\text{light}} - (k_{\text{SP}}^{\infty'} + \Delta k'_{\text{SP}}) - \mathrm{i}(\Gamma^{\infty} + \Gamma^{\text{rad}})} \tag{4.8}$$

Eq. (4.5) shows that there is a possibility to adjust k_{xa}^{light} with θ or ω. The SP resonance condition is thus attained by varying either the angle of incidence or the frequency to match the thin-film perturbed real part of the x-component of the SP wave to fulfil $k_{xa}^{\text{light}} = k_{\text{SP}}^{\infty'}$. Under these conditions r_p has a minimum at the SP resonance. Ideally $r_p = 0$ if the metal thickness is tuned so that $\Gamma^{\infty} = \Gamma^{\text{rad}}$ and the resonance is then Lorentzian broadened.

In ellipsometry the angle of incidence and/or wavelength dispersion in Δ and Ψ are of interest. Close to an SP resonance Eq. (4.8) gives

$$\rho = \frac{r_p}{r_s} = \frac{r_{01p}}{r_s}\frac{k_{xa}^{\text{light}} - (k_{\text{SP}}^{\infty'} + \Delta k'_{\text{SP}}) - \mathrm{i}(\Gamma^{\infty} - \Gamma^{\text{rad}})}{k_{xa}^{\text{light}} - (k_{\text{SP}}^{\infty'} + \Delta k'_{\text{SP}}) - \mathrm{i}(\Gamma^{\infty} + \Gamma^{\text{rad}})} \tag{4.9}$$

where ρ is the complex reflectance ratio and r_s the s-reflection coefficient. From Eq. (2.10) it follows

$$\tan\Psi = \frac{|r_{01p}|}{|r_s|}\sqrt{1 - \frac{4\Gamma^{\infty}\Gamma^{\text{rad}}}{Q^2 + (\Gamma^{\infty} + \Gamma^{\text{rad}})^2}} \tag{4.10}$$

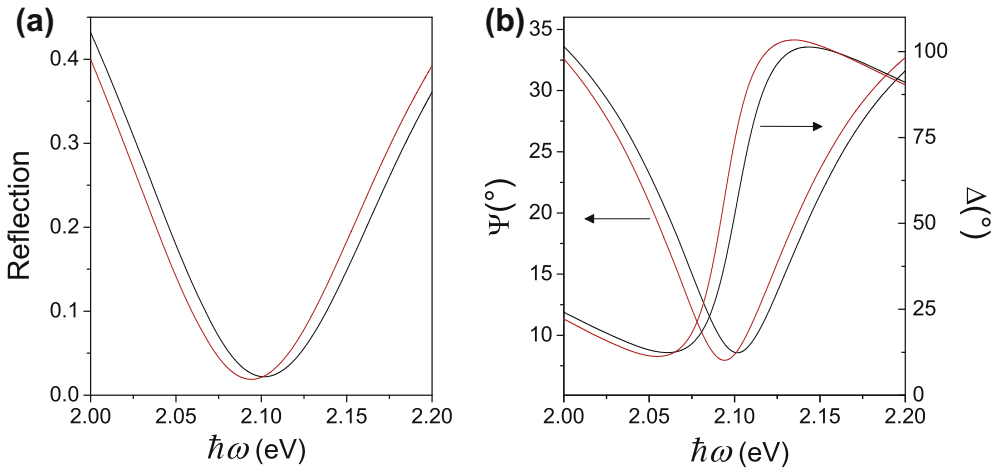

Fig. 10. A comparison of (a) the standard SPR response with (b) the SPR-ellipsometry parameters. Black lines are for a 45.1 nm gold film on glass in water at 76.2 degrees incident angle, and red lines are with a 1 nm thick layer ($\varepsilon = 2.25$) added. (For interpretation of the references to colour in this figure legend, the reader is referred to the web version of this article.)

$$\Delta = \arg\frac{r_{01p}}{r_s} + \arctan\frac{2Q\Gamma^{\mathrm{rad}}}{Q^2 + (\Gamma^{\infty} + \Gamma^{\mathrm{rad}})(\Gamma^{\infty} - \Gamma^{\mathrm{rad}})} \tag{4.11}$$

where $Q = k_{xa}^{\mathrm{light}} - (k_{\mathrm{SP}}^{\infty\prime} + \Delta k'_{\mathrm{SP}})$. Neither r_{01p} and r_s are involved in the SP and are slowly varying functions of k_{xa}^{light} around the SP resonance. The dispersion in $\tan\Psi$ is dominated by the expression under the square root in Eq. (4.10). Often Ψ is shown and close to the resonance $\tan\Psi \approx \Psi$ for small Ψ. The dispersion in Δ is dominated by the second term in Eq. (4.11). If the metal layer thickness is matched for zero reflectance, i.e., $\Gamma^{\infty} = \Gamma^{\mathrm{rad}}$, then Eq. (4.11) reduces to

$$\Delta = \arg\frac{r_{01p}}{r_s} + \arctan\frac{2\Gamma^{\mathrm{rad}}}{k_{xa}^{\mathrm{light}} - (k_{\mathrm{SP}}^{\infty\prime} + \Delta k'_{\mathrm{SP}})} \tag{4.12}$$

Eq. (4.12) shows that, at an SP resonance, i.e., $k_{xa}^{\mathrm{light}} = k_{\mathrm{SP}}^{\infty\prime} + \Delta k'_{\mathrm{SP}}$, Δ is a step function with step π if k_{xa}^{light} is varied by scanning either ω or θ_a over the resonance.

In a real measurement non-idealities such as surface and interface roughness, or imperfectly matched metal layer thickness, will come into play. If a small mismatch $\Delta\Gamma = \Gamma^{\infty} - \Gamma^{\mathrm{rad}}$ is introduced, Eq. (4.12) becomes

$$\Delta = \arg\frac{r_{01p}}{r_s} + \arctan\frac{1}{\frac{k_{xa}^{\mathrm{light}} - (k_{\mathrm{SP}}^{\infty\prime} + \Delta k'_{\mathrm{SP}})}{2\Gamma^{\infty}} + \frac{\Delta\Gamma}{k_{xa}^{\mathrm{light}} - (k_{\mathrm{SP}}^{\infty\prime} + \Delta k'_{\mathrm{SP}})}} \tag{4.13}$$

When $k_{xa}^{\mathrm{light}} = (\omega/c)\sqrt{\varepsilon_a}\sin\theta_a$ is varied by scanning either ω or θ_0 over the SP resonance, the variation of Δ is dominated by the behaviour of argument of the arctan function in the second term in Eq. (4.13). If $\Delta\Gamma$ is made very small by carefully controlling the metal film thickness, a sharp resonance will occur in a frequency interrogation when $\omega = \omega_{res}$ where subscript *res* indicates the SP resonance values.[4]

A comparison of the standard SPR response with the SPR-ellipsometry parameters is presented in Fig. 10 for a 1 nm thick layer ($\varepsilon = 2.25$) on a 45.1 nm gold film on glass in water at 76.2 degrees incident angle. Near the resonance the Ψ response is not only sharper but also the Δ response gives additional sensitivity which may be modelled to provide information about the surface layer. Several

[4] The angle of incidence is then assumed to be at θ_{res}. In an angle of incidence interrogation the resonance occurs in an angle scan when $\theta = \theta_{\mathrm{res}}$ if the frequency is set at $\omega = \omega_{\mathrm{res}}$.

biosensor applications have been suggested for SPR-ellipsometry but so far there are few applications outside academic research. Current research involves imaging to allow high throughput screening [103]. A main advantage for biosensing is the increased sensitive compared to ordinary SPR methodology but often applicability is not sensitivity limited. In most cases the biochemical specificity is limiting and unwanted bioadsorption above detection limits of SPR instruments occurs. There is thus no need for the improved capability of SPR-ellipsometry especially as it technically is more complex. A promising recently suggested application is gas sensing based on SPR-ellipsometry. Nooke et al. [104,105] have shown that ellipsometry using SPR enhancement in thin gold films can be used to detect and monitor hazardous gases. They used various coatings on the gold film and detection limits below 100 ppm were found for methane, propane and carbon dioxide and below 10 ppm for hydrogen.

5. Particle plasmon resonances

The bulk plasmon resonance discussed in Section 3 can be predicted using the Airy equations (2.16), which may be derived by solving Maxwell's equations for planar geometry. If we move away from the planar geometry to spherical geometry, the symmetry demands that excitation of the resonance no longer depends on the direction of the incident light. A spherical solution to Maxwell's equations was presented by Mie which accurately predicts the resonance frequency of spherical metal particles. These resonances go variously by the names localized SPR, localized SPP, Mie plasmon polaritons, particle plasmon polaritons, and particle plasmon resonances.[5] After the descriptions by Faraday, the relation between the size of the particle and the observed colour was part of extensive investigation in the 19th century. A first success was Maxwell Garnett's theory (MGT) in 1904 relating the change in colour to the polarizability of a particle and the optical properties of the ambient [106,107]. The MGT holds for the long wavelength approximation but fails when the particle size increases such that retardation (phase) effects become important. In 1908, Gustav Mie solved Maxwell's equations for spherical geometry, providing the modern version of the theory of scattering and absorption of electromagnetic radiation by a sphere [108].

5.1. Isolated spherical particles

5.1.1. The quasistatic approximation

The Mie solution predicts the absorption and scattering properties for particles of arbitrary size. For small particles it is well approximated by a sum of multipolar resonances with varying size-dependent strengths. In the quasistatic limit (Rayleigh limit) one may ignore the effects of the phase variation of the electric field at different points on the particle (retardation) and the dipolar oscillation mode dominates the response. For a spherical particle, surrounded by a medium with dielectric constant ε_a, the polarizability α (defined as $\mathbf{p} = \varepsilon_a \alpha \mathbf{E}_0$, where $\mathbf{p}$ is the dipole moment) in the dipolar limit is

$$\alpha = 4\pi\varepsilon_0 a^3 \frac{\varepsilon_m - \varepsilon_a}{\varepsilon_m + 2\varepsilon_a} \tag{5.1}$$

where a is the radius of the particle, $\varepsilon_m(\omega) = \varepsilon'_m + i\varepsilon''_m$ is the dielectric function of the metal sphere. Thus, provided ε'' is small or weakly dependent on ω, a resonance occurs if $\varepsilon'_m = -2\varepsilon_a$. This is known as the *Fröhlich condition* [60].

For a Drude metal with a dielectric function as given in Eq. (3.7), the Fröhlich condition leads to the particle plasmon resonance frequency,

$$\omega_{\mathrm{pp}}^2 = \frac{\omega_p^2}{\varepsilon_\infty + 2\varepsilon_a} - \Gamma^2 \tag{5.2}$$

For a pure Drude metal with $\varepsilon_\infty = 1$ and $\Gamma \ll \omega_{\mathrm{p}}$ in air ($\varepsilon_a \approx 1$) one obtains $\omega_{\mathrm{pp}} = \omega_p/\sqrt{3}$ [60]. For gold ($\varepsilon_\infty = 10$) and silver ($\varepsilon_\infty = 4$), the actual resonance frequency is considerably reduced.

[5] As discussed in the previous section, the term *polariton* refers to a photon coupled to a quasiparticle such as a plasmon. Particle plasmon resonances and bulk plasmon resonances are not coupled to photons and decay due to damping with a characteristic time constant when the external stimuli is removed.

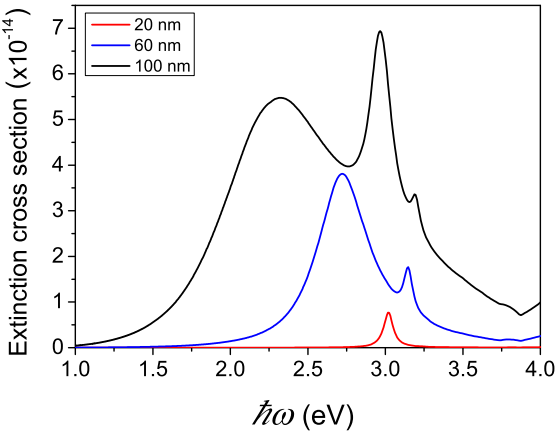

Fig. 11. Calculated extinction cross sections for single silver spheres using the Mie theory.

Fig. 11 shows the spectral plane-wave extinction cross-sections of silver particles of 20, 60 and 100 nm diameter in glass, calculated using the MiePlot software [109]. The quasistatic approximation is valid for the 20 nm particle and only a dipolar mode is observed. At larger diameters, the dipolar mode is redshifted due to retardation. The quadrupolar mode is already visible in the 60 nm particle on the high-energy side of the dipolar mode. In the 100 nm particle the quadrupolar mode is stronger than the dipolar mode and the octupolar mode is visible. The broadening of the dipolar oscillation also increases with particle size, both in Mie theory and experimentally [110]. The broadening occurs due to a dephasing of the plasmon, arising from both radiative and non-radiative (absorption) relaxation channels. In the dipolar-dominated small size limit the particle may be considered as a classical oscillating dipole and the absorbed photons are thus efficiently reradiated. As the particle size increases the radiative processes are retarded and absorption processes increase.

5.1.2. Small particle broadening

The absence of a size dependence in Eq. (5.2) implies that the resonance should not change for particles below the quasistatic limiting diameter of around 20 nm. In practice, for 5 nm particles the resonance is strongly damped and for particles below around 2 nm it completely disappears [111]. This is understood in the context of the increase of the Drude broadening parameter, Γ, by effects such as impurities, lattice defects and surface scattering [60]. Note that quantum effects for metal particles are not apparent for particles with more than a few hundred atoms, which corresponds to a diameter below 1 nm [60]. For a bulk crystal, the mean free path l_∞ is determined by electron and phonon interactions. This length scale reflects the distance between memory cancelling collisions of the electrons. As long as these collisions are slightly inelastic, the interaction involves electrons close to the Fermi surface and hence:

$$\Gamma_\infty = \frac{v_F}{l_\infty} \tag{5.3}$$

Here v_F is the Fermi velocity of the electrons. For a small particle with radius a the effect is empirically accounted for by introducing an additional term into the broadening [112]:

$$\Gamma(R) = \Gamma_\infty + \frac{A v_F}{a} \tag{5.4}$$

The parameter A accounts for the spherical nature and can as well account for the influence of the chemical environment. For a spherical particle with no chemical effects, $A = 4/3$ [60] [113]. The chemical effect on the A parameter may be determined experimentally by comparing the broadening with microstructural analysis of the particle size. While the broadening can be determined using

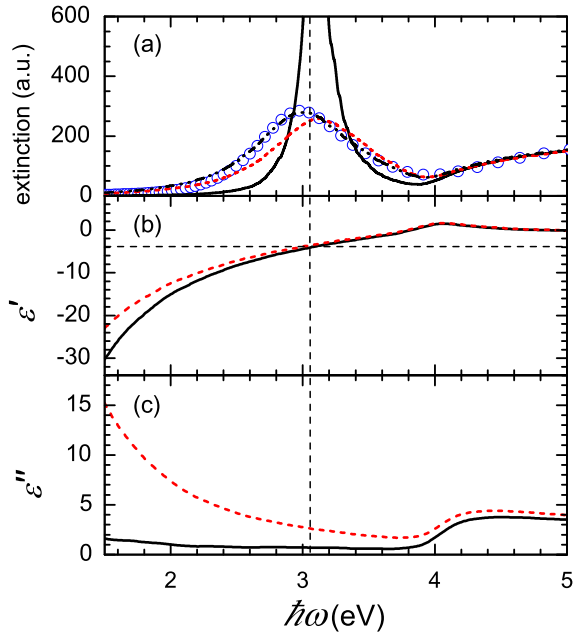

Fig. 12. (a) The measured extinction spectrum of 5 nm diameter silver nanoparticles with a 2 nm dodecanethiol shell suspended in hexane (blue circles). Also shown are the calculation of the particle extinction derived from the silver dielectric function shown in (b) and (c) for bulk silver (black solid lines) and with a reduced electron mean free path (red dashed lines). The result of the dodecanethiol shell and the hexane solution are also shown (black dashed line) (Adapted from [119]). (For interpretation of the references to colour in this figure legend, the reader is referred to the web version of this article.)

reflection and transmission measurements [114] it can also be determined using spectroscopic ellipsometry. The method is generally only useful for well-dispersed particles suspended in a film of transparent media such as glass or polymer. Dalacu and Martinu analysed SE data from co-sputtered Au/SiO_2 films and compared the resonance to the size determined from transmission electron microscopy to determine $A = 0.16$ [115]. They also investigated plasma-polymerized fluorocarbon / gold composites and determined a $A = 0.25$ Dalacu [116]. Dynamic SE was used to observe the growth of silver nanoparticles in polymer thin films by temperature induced reduction of silver salts[117,118]. By determining a final $A = 0.41$ using scanning electron microscopy, the data could be modelled to give the particle radius during growth. The plasmon resonance was completely broadened for particles smaller than about 2 nm due to surface damping. For the analysis of a thin film obtained from the deposition of nanocolloidal particles that are prepared prior in a fluid solution, an extinction spectrum of the particle solution can be used to extract the change in dielectric function as a result of the limited size of the colloids. An example of this is shown in Fig. 12 for silver colloids [119]. A modification of the Drude part of the dielectric function as given by Eq. (5.4) and displayed in Fig. 12 allows a good simulation of the measured extinction spectrum. A similar characterisation was also performed for nanocolloidal Au particles [120,121].

5.2. Effective medium theories

When moving from the case of an individual particle to a large ensemble of particles we must take into account the collective behaviour of the particles in a medium and their affect on each other. By treating the material as having a spatially homogeneous *effective* permittivity the Fresnel equations and those of geometrical optics may still be applied. The effective medium concept reflects the fundamental connection between the macroscopic permittivity of a material and the microscopic

polarizabilities of the constituents. Aspnes gives an excellent contemporary review of effective medium theories in the context of plasmonics [122].

On a microscopic level, the polarization **P** in the constitutive relation (2.1) is the sum of the polarization of all atoms, molecules or particles in the medium with polarizability α, such that

$$\mathbf{P} = N_e \propto (\mathbf{E} + \mathbf{E}_{\text{ind}}) = N_e \propto E_{\text{eff}} \tag{5.5}$$

where N_e is the number of elements and $\mathbf{E}_{\text{eff}}$ is the effective field at the position of the element. The contribution of surrounding elements to the polarization is reflected by the local induced electric field, $\mathbf{E}_{\text{ind}}$. The effective permittivity of the material is calculated by determining the effective electric field due to all atoms on a single atom and then summing over all atoms. One method to do this is to find the field at the centre of a spherical volume (Lorentz cavity) in a dielectric with permittivity ε, which is [123]

$$\mathbf{E}_{eff} = \mathbf{E} + \frac{\mathbf{P}}{3\varepsilon_0} \tag{5.6}$$

Introducing Eqs. (2.1) and (5.5) yields the Clausius–Mossotti relation.

$$\frac{\varepsilon - 1}{\varepsilon + 2} = \frac{N_e \alpha}{3\varepsilon_0} \tag{5.7}$$

The Lorentz-Lorenz effective medium expression uses this approach to relate the optical polarizability of gas molecules to the refractive index of a gas mixture [124]. It accounts very well for the effect of gas pressure, temperature and composition. However, it did not solve the problem of understanding the coloration of glass by metal nanoparticles; a widely discussed topic at that time.

5.2.1. Maxwell Garnett theory

Maxwell Garnett extended the Lorentz-Lorenz approach from the atomic case to account for spherical particles in a dielectric medium [106,107]. The Maxwell Garnett theory (MGT) uses the Rayleigh formulas and takes the first order approximation of this relation, i.e., all particles give a similar change to the dielectric function and the change in the dielectric function of the host is negligible with the inclusion of more particles. Under these conditions, an ensemble of particles in the quasistatic limit, have an effective dielectric function, ε_{eff}

$$\frac{\varepsilon_{eff} - \varepsilon_a}{\varepsilon_{eff} + 2\varepsilon_a} = F\frac{\varepsilon_m - \varepsilon_a}{\varepsilon_m + 2\varepsilon_a} \tag{5.8}$$

where F is the volume fraction of the particles in the medium. The first order approximation explains the limited F range in which the MGT can be used. Usually only a few percent is used as a limit, although practically good agreement with experiment is found for up to $F = 0.3$. The MGT has been used extensively to model the dielectric functions of metal/dielectric composites (especially CerMets – ceramic/metal composites). A good example of an ellipsometry application is the work of Palpant et al. [125], who determined the isotropic n and κ of very small gold clusters (2 - 4 nm average size) embedded in alumina matrix formed by CW laser evaporation via the MGT. In this size range the effects of a modified broadening due to increased surface scattering are important. Cho et al. performed a similar study of alternately sputtered Au/SiO2 [126].

We should expect that in the limit of very small F the MGT converges to the quasistatic Mie case (Eq. (5.2)). For metallic spheres with a Drude dielectric function (Eq. (3.7)), Eq. (5.8) describes a Lorentzian with a resonance frequency of

$$\omega_0^2 = \frac{\omega_p^2(1 - F)}{\varepsilon_\infty + 2\varepsilon_a} \tag{5.9}$$

This formula converges in the limit $F \to 0$ with Eq. (5.2) as expected. As F increases the MGT predicts a red-shift of the resonance frequency. This is logical since the resonance frequency of a Drude metal is zero, which would be the case in the limit $F \to 1$.

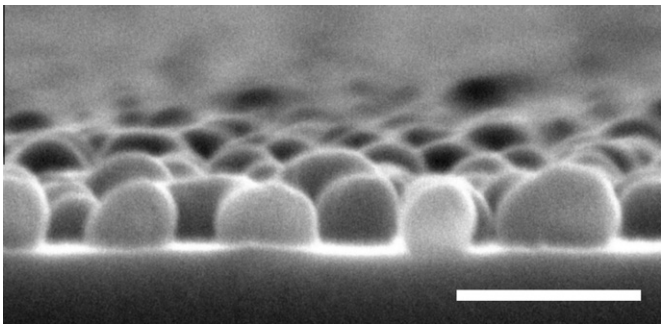

Fig. 13. Side view SEM of a silver metal island film (MIF) deposited on SiO_2 by magnetron sputtering at room temperature. The particles are truncated spheroids. Scale bar is 100 nm.

5.2.2. The MGT in ellipsometry

The Lorentzian shape of the resonance in the MGT for a Drude metal in a dielectric can be used as a quick approximation to determine the dielectric function from ellipsometric data without explicitly fitting *F* or other unknowns. Yamaguchi was one of the first to note this [127]. He observed resonance type absorption in discontinuous evaporated noble metal island films (MIFs) (Fig. 13) and used the MGT to derive a Lorentzian expression for the resonance.[6] This Lorentzian depends on the fill factor of the material, and the energy position of the resonance maximum depends only on *F*, according to Eq. (5.9). It can therefore be used to determine the area coverage of the metal film. Doremus [128] exploited this dependence in a similar approach and derived an equation that predicts the resonance maximum in island films of noble metals using the measured bulk dielectric functions of the metal. The maximum is expected to occur when the real part of the dielectric function is related to:

$$\varepsilon'_m = -\frac{(2+\phi)n_d^2}{1-\phi} \tag{5.10}$$

where ϕ is the projected surface area coverage of the particles on the substrate, and n_d is the refractive index of the substrate. The expected maximum frequency as a function of the surface coverage for a silver MIF is plotted in Fig. 14. Also shown is the prediction of the thin island film (TIF) theory (discussed below). Doremus later empirically demonstrated the applicability of Eq. (5.10) using a wide array of published results for various discontinuous metal films [129]. Wormeester et al. showed the effect of ε_∞ on the resonance position and broadening [130].

Using spectroscopic ellipsometry, a large number of authors have applied the simple Lorentz oscillator approach to determine the dielectric function of gold nanoparticle/organic films [131–133], electrodeposited gold on anodized and etched Al and Cu films [134], nanoporous silver [135], gold [136] [137] and platinum [138], and hollow gold nanoparticles [139]. The applicability of the Lorentzian assumption and its limitations in the event of larger ϕ was demonstrated by Oates et al. using in situ real time spectroscopic ellipsometry (RTSE) on films deposited at room temperature and 150 °C [140]. Fig. 15 shows the effective dielectric functions of the island film deposited at 150 °C as a function of nominal film thickness, determined using both the Arwin-Aspnes method (Section 2.3.2) and a Lorentzian expression to approximate the MGT. As more material is deposited and the surface coverage increases, the plasmon resonance red shifts, grows in amplitude and broadens. The Lorentzian fit provides a good approximation of the plasmon frequency but not the broadening or amplitude. RTSE during the Volmer–Weber growth of MIFs)is a classic example of the power of ellipsometry for plasmonic investigations. After the early single wavelength experiments on silver [141], the development of multichannel detectors by the Collins group allowed full spectroscopic

[6] Yamaguchi assumed that $\varepsilon_\infty = 1$ which limited the application of his approach.

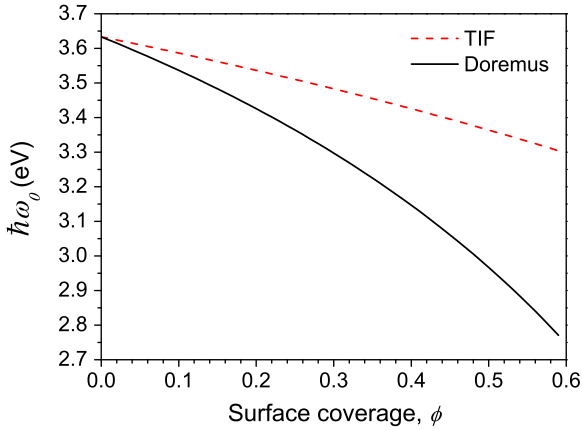

Fig. 14. Dependence of the plasmon resonance maximum in a MIF as a function of the surface area coverage, as predicted by Eq. (5.10) and the Thin Island Film (TIF) theory.

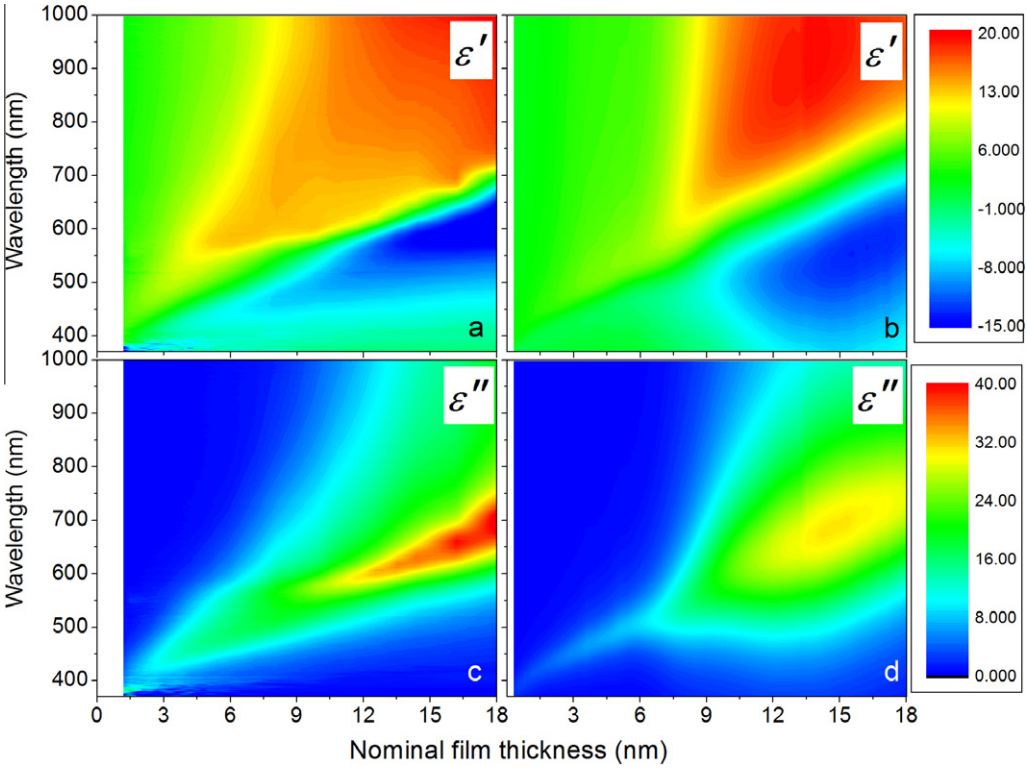

Fig. 15. Effective dielectric functions of silver island films from in situ RTSE. On the left (a,c) are the real and imaginary parts determined using the Arwin–Aspnes method (Section 2.3.2) whereas the right panels shows the data fit with a Lorentzian expression to approximate the MGT. In the lower panels ε'' clearly shows the plasmon resonance growing in amplitude and broadening as the surface coverage increases. The Lorentzian fit provides a good approximation of the plasmon frequency but not the broadening or amplitude.

measurements on aluminum with an MGT analysis [142,143], silver with a simple Lorentzian analysis [144–146] and gold using the Mie equations [147].

Whereas RTSE provides an extended data set in the time domain, intentionally creating films with a thickness gradient provides an extended data set in space. The gradient may be used as a library of particle sizes, shapes and spacings for a combinatorial investigation of the effect of these parameters on the optical properties using multiple analysis techniques. Bhat and Genzer used a chemical gradient to create a number density of gold nanoparticles on a substrate. They then used SE as a quick method to determine the particle density by comparing the maximum in the SPR from the ellipsometric phase data with the surface coverage determined from AFM and X-ray analysis [148]. Oates et al. compared the Raman enhancement from silver island films with the optical properties determined using SE. Additional information was taken from SEM images to compare the particle dimensions. The spatial resolution of the Raman results was around 1 μm, allowing identification of a dependence in the optimal enhancement morphology on the Raman laser wavelength [149]. The use of complimentary analysis methods is critical to provide information for the SE modelling, or to compare the predictions of the models. Common techniques are AFM [150] and electron microscopy [151], although the power of X-ray scattering (especially GISAXS) is becoming more accessible [152].

5.2.3. Percolation

The success of the MGT in the application to small metal particles stems from the fact that it is quite good in the prediction of the resonance energy. However, the MGT does not predict a percolation threshold. This results not just from the fact that it is small volume approximation. The MGT also uses a specific topology, i.e., the inclusion of spherical particles. The latter condition implies that for a 50% volume fraction, a change of the role of the host and the inclusion leads to a different result. Both of these limitations have been addressed by Bruggeman [153]. In his seminal paper several EMAs for different topologies are derived. The most widely used considers a material volume made entirely of two (or more) spherical inclusions of material b and c. This leads to the Bruggeman EMA formula:

$$F\frac{\varepsilon_b-\varepsilon_{eff}}{\varepsilon_b+2\varepsilon_{eff}}+(1-F)\frac{\varepsilon_c-\varepsilon_{eff}}{\varepsilon_c+2\varepsilon_{eff}}=0 \tag{5.11}$$

where F is the volume fraction of material b. In this expression, the particle and host media are interchangeable and it may be used to model higher volume fractions and percolation events. Although this expression and its 2D analogue [154] are valid for high volume fractions, this expression is not as accessible for an analytical expression of the plasmon resonance energy.

The study of percolating systems has an extensive history, with interest being particularly strong in the study of CerMets in the 1970s [155] and continuing to attract significant attention today [156]. With respect to discontinuous metal films, the percolation threshold may be defined as the point where the particles form a continuous network inside the matrix or, equivalently, the point at which the size of connected clusters diverges. For the purposes of deposited metal island films it is convenient to define the percolation threshold as a critical thickness, d_c, which is dependent on the Volmer–Weber growth conditions. Both the DC conductivity and the far-field optical response show unique characteristics at percolation. For this reason spectroscopic ellipsometry has been used widely to determine the percolation threshold and is complimentary to conductivity measurements ([39,140,157]). It is especially effective for investigating the applicability of percolation models due to the simultaneous determination of the dielectric function as well as the film thickness.

In MIFs of gold and silver the particle plasmon resonance, clearly observed in ε'', shifts to lower frequencies as d_c is approached. Well past d_c, extrapolation of ε'' to $\omega = 0$ gives an indication of the DC conductivity in accordance with Eq. (3.6), and ε' will give the static dielectric constant. Since the material undergoes a insulator-to-metal transition at percolation we may expect that ε' in the infrared region will transit from positive (as for an insulator) to negative at d_c. The experimental results in Fig. 16 from the work of Hövel et al. [158] show that ε' in fact rises as d_c is approached, then goes through a maximum at d_c before becoming negative. This fits well with percolation theory for low-frequency conductivity of percolating networks which predicts a divergence of the static dielectric constant at d_c according to

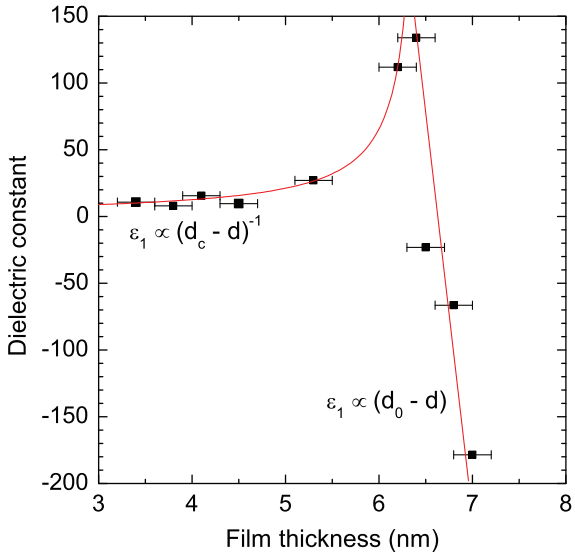

Fig. 16. Divergence of the static dielectric constant as a function of the nominal film thickness for gold deposited on Si/SiO_2. The solid lines correspond to Eq. (5.12) with $d_c = 6.4$ nm, $s = 1$ below percolation and $d_c = d_0 = 6.7$ nm and $s = -1$ above percolation (image courtesy of B. Gompf, from reference [158], Copyright (2010) by the American Physical Society).

$$\varepsilon'(0,d) \propto (d_c - d)^{-s} \tag{5.12}$$

where s is the critical exponent. At a small but non-zero frequency, ω, the divergence becomes a maximum according to

$$\varepsilon'(\omega,d) = \varepsilon_s \left(\frac{\sigma_m}{\omega \varepsilon_0 \varepsilon_s} \right)^{1-u} \tag{5.13}$$

where ε_s is the dielectric constant of the insulating component and σ_m is the real part of the conductivity of the metallic component. The critical exponents s and u are predicted to be 1 and 0.62, respectively, for a 3-D system and 1.3 and 0.5, respectively, for a 2-D system. An experimental value for s of between 1.1 and 1.7 was determined for 2-D titanium films using spectroscopic ellipsometry [39].

A parametric model for the dielectric function close to and above percolation is not straightforward due to the complexity of the material nanostructure. Below percolation a resonant component (Lorentzian) should be incorporated for the particle plasmon resonance. Above percolation the frequency of this resonance will tend toward zero (i.e., the Drude free electron model) [145], however it is logical that very close to d_c both the plasmon resonance and the free electron behaviour should co-exist [158]. This is especially important when modelling the optical properties of nanoporous metallic films [154,156].

5.3. Anisotropic particle resonances

5.3.1. Elliptical particles

The Mie solution is derived for a spherical particle. It is straightforward to extend the approach to an ellipsoidal geometry in the quasistatic limit. The deviation from spherical symmetry results in splitting of the plasmon resonances in isolated nanoparticles. Noble metal nanorods exhibit two prominent plasmon peaks with frequencies dependent on the aspect ratio (length/width), as well as the influences described above for spherical particles. To account for the shape anisotropy Gans [159] provided an extension to the Mie formulas in the quasistatic limit by splitting the polarizability into Cartesian components. Eq. (5.1) then becomes [160]

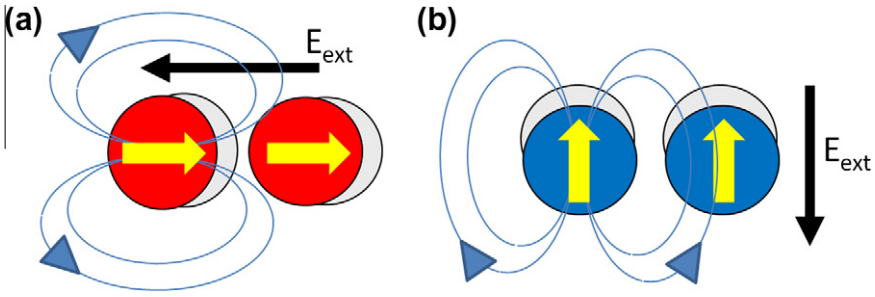

Fig. 17. Dipole coupling between neighbouring nanoparticles. An external field polarizes a particle, creating an internal dipole moment (yellow arrow) and a dipole field (blue lines). At a neighbouring particle the dipole field either (a) subtracts from the external field, red shifting the resonance frequency, or (b) adds to the external field, blue shifting the resonance energy. The effect is reciprocal and in a metal island film two polarization-dependent resonances will be observed. (For interpretation of the references to colour in this figure legend, the reader is referred to the web version of this article.)

$$\alpha_i = \frac{4\pi\varepsilon_0 abc(\varepsilon_m - \varepsilon_a)}{3\varepsilon_a + 3L_i(\varepsilon_m - \varepsilon_a)} \tag{5.14}$$

and introducing a depolarization factor, L_i, where the subscript i denotes the three principle axes of the ellips, x, y, z, (x being the long axis) and a, b and c are the length of the ellipsoid in those directions, respectively. The depolarization factors are

$$L_x = \frac{1-e^2}{e^2}\left(-1 + \frac{1}{2e}\ln\frac{1+e}{1-e}\right); \tag{5.15}$$

$$L_{y,z} = \frac{1-L_x}{2}; \tag{5.16}$$

where e is the rod ellipticity $e^2 = 1\text{-}(b/a)^2$. One should note that since the Gans formula is based on the quasistatic assumption the particle major axis should not be significantly greater than around 20 nm. Larger and more complex shaped particles exhibit multiple resonances peaks and further lifting of degeneracy due to asymmetrical shapes. Lamarre et al. incorporated the Gans equations into the MGT and applied it for the SE analysis of gold particles in SiO_2 bombardment by heavy ions where the nanoparticles were elongated in the direction of the ion velocity [161].

5.3.2. Dipole coupling

In many practical cases the nanoparticles under investigation are in close proximity to one another and the electric fields generated by the polarized particles interact strongly with adjacent particles. Consider the simple case of a dimer of metallic nanoparticles in the quasistatic limit excited by an electric field parallel to the dimer axis (Fig. 17(a)). If the particle separation is small the electric fields generated by the plasmonic dipoles will reduce the restoring force on the electrons in the neighbouring particle, thereby red-shifting the resonance frequency. Conversely, if the external field is perpendicular to the dipole axis (Fig. 17(b)) the dipole fields will blue-shift the resonance frequency. Since the effect of each particle on the other is reciprocal the plasmons hybridize [162]. In the large-gap limit the effect is akin to the interaction between two isolated dipoles, whilst for small gaps the effects of higher order multipoles come into play. The electric fields are highly concentrated in the gap, increasing with a reduced gap distance. This is the origin of the extreme enhancement factors observed in surface-enhanced Raman scattering (SERS) experiments [5].

Extending the concept to a layer of isolated densely-packed particles on a surface, it is clear that the plasmon resonance in the in-plane direction will be red-shifted with respect to the out-of-plane resonance. Maxwell-Garnett already noted that the dielectric function, ε_z, of a film of nanoparticles may be different from ε_x, and "if so, the film behaves optically like a uniaxial crystal"[163]. This results in a splitting of the plasmon resonance. The two modes; a low-energy absorption parallel to the

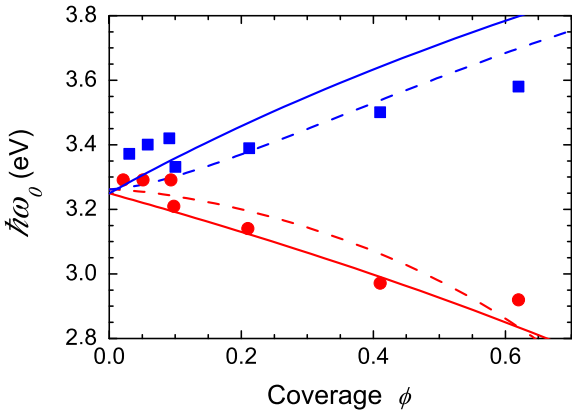

Fig. 18. The energy of the plasmon resonance maximum for the in-plane (*a*-mode) (red symbols/lines) and out-of-plane (*c*-mode) (blue symbols/lines). The lines show the prediction of the TIF theory for hexagonal distribution (dashed), and isotropic distribution (solid). The data points are taken from [114]. (For interpretation of the references to colour in this figure legend, the reader is referred to the web version of this article.)

substrate surface (*a*-mode) and a high energy absorption normal to the substrate surface (*c*-mode), are easily observed in the reflection spectrum of p-polarized light at large angles from the surface normal [164,165]. The position of the resonances depends strongly on ϕ, as shown in Fig. 18. This plot shows experimental data from [114] compared with simulation of the TIF theory (discussed below). Splitting is first observed at $\phi \approx 0.1$. As ϕ increases toward unity the *a*-mode resonance red-shifts toward $\hbar\omega = 0$ and the *c*-mode resonance blue-shifts toward the screened plasma frequency, $\hbar\omega_{ps}$. One may intuitively consider this as the *a*-mode shifting toward the Drude case as the film percolates and in-fills, and the *c*-mode shifting toward the volume plasmon case as the geometry moves from an array of spheres to an ultrathin slab.

Although alluded to in the original work, the peak splitting is not predicted by the Maxwell-Garnett formalism, and the effect of the dipole interaction will significantly alter the prediction of the resonance frequency in the *a*-mode resonance. In fact, the situation is somewhat more complicated when the particles are in proximity to a surface since the particles are rarely spherical, but tend to be truncated oblate spheroids, especially for evaporated or plasma deposited films (Fig. 13). An additional factor due to the substrate is the breaking of symmetry of the surrounding medium and the effect of substrate interactions (or image effects). The presence of the interface results in the formation of an image of the metal particle across this interface. In the dipole approximation, this is described by the generation of an image dipole in the substrate [166,167]. For higher coverage, the interaction between the images of neighbouring dipoles also has to be considered. This effect is even more important for oblate particles. As a result, the resonance frequency can be considerably reduced.

Eq. (5.2), which was derived for isolated non-interacting spherical particles, may be generalized for interacting non-spherical particles on a surface to:

$$\omega^2 = \frac{\omega_p^2}{\varepsilon_\infty + k_s \varepsilon_a} - \Gamma^2 \tag{5.17}$$

where k_s is the screening parameter. The above expression is the general case of Eqs. (4.3), (5.2) and also of Eq. (5.9) (for $F = 1$). $k_s = 2$ for non-interacting spherical particles. If the observed anisotropy is caused purely by the particle shape then k_s is related to the depolarization factor in Eq. (5.14) via $k_s = (1 - L)/L$. This effect also leads to a split of the resonance energy. However if the particle density is high enough that the dipolar interactions become significant then one cannot discern the relative contributions from the shape and coupling effects. The same is true for the image dipole.

Peak splitting is observed in oblique-angle reflection measurements of p-polarized light of dense nanoparticle films and is thus accessible by SE measurements. To unambiguously determine the

z-component requires measurements at multiple oblique-angles [168]. The effect of the image dipole of a particle on the collective optical response was explicitly incorporated into a simple dipolar model by Yamaguchi [169]. Truong et al. performed measurements of the anisotropy in aggregated gold films, looking at the component of the dielectric function normal to the surface by performing multiple angle measurements. The results were modelled using a modified Yamaguchi approach, with the substrate image dipoles explicitly incorporated [170]. Anisotropy was also studied using the Yamaguchi theory by Toudert et al. in their work on quantitative modelling of the surface plasmon resonances of silver nanoclusters sandwiched between Si_3N_4 layers [151]. Their thorough analysis investigated the influence of nanocluster size, shape and organization as measured by transmission electron microscopy, with the anisotropic optical properties determined using variable angle spectroscopic ellipsometry. They conclude that the spectral position of the plasmon resonance appears to be mainly affected by the average shape of the clusters, and weakly by their size, their shape distribution and the electromagnetic interaction between them.

5.3.3. Thin Island film theory

At the same time as the Yamaguchi work appeared, Bedeaux and Vlieger presented an alternative approach [171]. The polarizability of (identical) particles on a surface is modified to an effective polarizability of each particle. The image effect leads to an effective polarizability that differs for the direction parallel and perpendicular to the interface. The incorporation of the image effect was the start for the development of the so-called Thin Island Film (TIF) theory by Bedeaux and co-workers [172] which also incorporates the neighbour interaction effect and the description of non-spherical particles. This TIF theory is in principle a multipole expansion of the electro-magnetic problem of the response of identical particles by an incident electric field. However, as shown by Haarmans et al. [173] a noble metal particle film with a coverage up to 50% is well described by dipole and quadrupole terms. Wormeester et al. [119] showed that if image effects are negligible, dipolar terms are sufficient to describe the optical response in this coverage range. A computer program that calculates the optical response with the TIF theory up to arbitrary order, called GRANFILM, has been published by Lazarri and Simonsen [174].

The collective optical effect of a deposited ensemble of particles is expressed by the so-called excess dipole strength, γ and β, parallel and perpendicular to the interface, respectively, described by:

$$\gamma = \phi 4a\varepsilon_a \frac{\varepsilon_m - \varepsilon_a}{\varepsilon_m + k_{s,p}\varepsilon_a} = \phi \frac{4a\varepsilon_a}{3} \frac{\delta\varepsilon}{1 + L_p\delta\varepsilon} \tag{5.18a}$$

$$\beta = \frac{\phi 4a}{\varepsilon_a} \frac{\varepsilon_m - \varepsilon_a}{\varepsilon_m + k_{s,z}\varepsilon_a} = \phi \frac{4a}{3\varepsilon_a} \frac{\delta\varepsilon}{1 + L_z\delta\varepsilon} \tag{5.18b}$$

$\delta\varepsilon = (\varepsilon_m - \varepsilon_a)/\varepsilon_a$ is referred to as the dielectric contrast. For non-interacting spherical particles without image effects, the screening parameter $k_{s,p} = k_{s,z} = 2$ for the parallel (p) and perpendicular (z) direction to the interface. The depolarization parameters L_p and L_z are 1/3 in this case.

The effect of interacting particles was studied by Barrera et al. [175]. They considered the particles placed on a lattice with r_0 the nearest neighbour distance. The depolarization factor for the two directions is:

$$L_p = \frac{1}{3}\left(1 - \frac{1}{2}\left(\frac{a}{r_0}\right)^3 S\right) \tag{5.19a}$$

$$L_z = \frac{1}{3}\left(1 + \left(\frac{a}{r_0}\right)^3 S\right) \tag{5.19b}$$

with S the result of the weighted sum over all lattice sites. For a lattice normalized to the nearest neighbour distance, this summation is given by $S = \Sigma 1/r^3$. For a hexagonally closed packed lattice $S = 11.034$ whereas $S = 9.03$ for a cubic lattice. Note that this neighbour interaction has no effect on the sum of the depolarization factors, $2L_p + L_z = 1$. Fig. 19 shows the effect of surface coverage for a

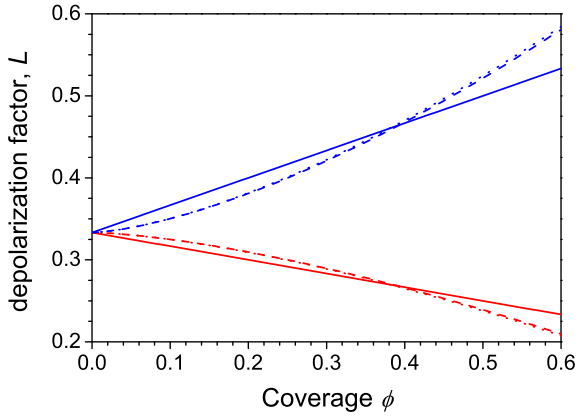

Fig. 19. Depolarization factors, L_p (blue lines) and L_z (red lines) as a function of surface coverage for a hexagonal lattice (dashed), a square lattice (dotted) and uniform distribution (solid line). (For interpretation of the references to colour in this figure legend, the reader is referred to the web version of this article.)

hexagonal lattice (dashed), a square lattice (dotted) and uniform distribution (solid line) on the depolarization factor. The change in the depolarization factor as a result of collective interaction results in a separate resonance energy for the parallel and perpendicular component according to Eq. (5.17). This interaction thus creates an effective polarizability that mimics an oblate particle. The split in resonance energy depends on the coverage and explains qualitatively the effect on the resonance energy as shown in Fig. 18. An approximation of the shift in resonance energy is shown.

The image effect gives an additional change to the depolarization factors. Haarmans and Bedeaux [176] derived an explicit form up to quadrupole order for these effects on the excess dipole strength γ and β:

$$\gamma_{qu} = \phi \frac{4a\varepsilon_a}{3} \frac{\delta\varepsilon\left(1 + L1_p\delta\varepsilon\right)}{\left(1 + L_p\delta\varepsilon\right)\left(1 + L1_p\delta\varepsilon\right) + \Lambda_p\delta\varepsilon^2} \tag{5.20a}$$

$$\beta_{qu} = \phi \frac{4a}{3\varepsilon_a} \frac{\delta\varepsilon(1 + L1_z\delta\varepsilon)}{(1 + L_z\delta\varepsilon)(1 + L1_z\delta\varepsilon) + \Lambda_z\delta\varepsilon^2} \tag{5.20b}$$

Here, L_p and L_z represent the dipolar correction terms and $L1_p$ and $L1_z$, Λ_p and Λ_z are the quadrupole depolarization factors. The definition of these terms as a function of surface coverage is provided in the appendix. The factors Λ_p and Λ_z are quite small and are only present if image effects play a role. Very often, Λ_p and $\Lambda_z \ll 1$ in a coverage range up to 50%. In this case the quadrupole contribution vanishes, and only the dipole contribution remains.

5.3.4. The incorporation of TIF in ellipsometry

The effect of the excess polarizabilities γ and β on the optical response can in a first approach be related to the so-called Drude thin film approximation, whose derivation already appears in the work of Rijn van Alkemade [177]. The thin film approximation describes the influence on the optical response by a thin film with thickness d that has an uniaxial dielectric function $\varepsilon_{//}$ and $\varepsilon_\perp$ that are a function of the height (z) above the substrate. The change in optical response is proportional to the integral value J:

$$J = \int_0^d \varepsilon_{\parallel}(z) - \varepsilon_a + \varepsilon_a\left(\frac{1}{\varepsilon_\perp(z)} - \frac{1}{\varepsilon_a}\right)dz. \tag{5.21}$$

Lekner argued that ellipsometry is only sensitive to the value of this so-called invariant J, but not to the specific details of the variation of the dielectric function, either parallel or perpendicular to the interface with position in the film z [178]. Bedeaux and Vlieger showed that

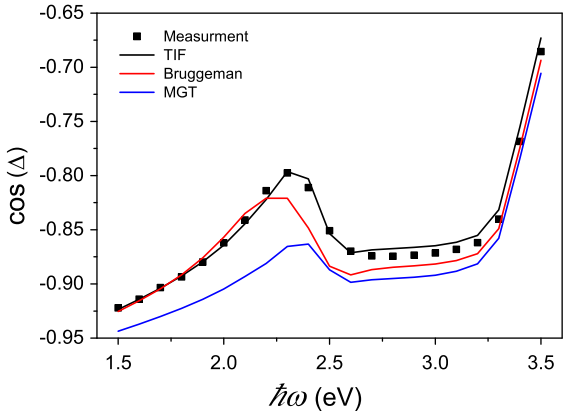

Fig. 20. Measured and theoretical dependence of the cosine of the ellipsometric phase angle, Δ, on photon energy for a silicon substrate covered with 13.6 nm diameter gold colloids.

$$J = \gamma + \varepsilon_a \varepsilon_s \beta \tag{5.22}$$

This enables a first evaluation of the optical response. However, as shown by Wormeester et al. [130], the coupling between the thin layer and substrate has to be taken into account in a more rigorous way. For this the coupling in terms of the Abelés matrix formalism described by Bohmer et al. [179] has to be used. This coupling uses the polarization dependent reflection and transmission coefficients for a thin island film. For s-polarized light

$$r_\ell^s = \frac{X^s}{1 - X^s} \text{ and } t_\ell^s = \frac{1}{1 - X^s} \tag{5.23}$$

with

$$X^s = \frac{i\omega\gamma}{2n_0 cos(\theta_0)}$$

and for p-polarized light

$$r_\ell^p = \frac{X^p}{1 - X^p} - \frac{Y^p}{1 - Y^p} \quad \text{and} \quad t_\ell^p = 1 + \frac{X^p + Y^p - 2X^pY^p}{(1 - X^p)(1 - Y^p)} \tag{5.24}$$

with

$$X^p = \frac{i\omega\beta(n_0)^3 \sin^2(\theta_0)}{2\cos(\theta_0)} \text{ and } Y^p = \frac{i\omega\gamma cos(\theta_0)}{2n_0}.$$

The Abelés film matrix for the interface reflection of a particulate film in terms of these reflection and transmission coefficients is given by

$$\mathbf{F} = \frac{1}{t_\ell}\begin{pmatrix} 1 & -r_\ell \\ r_\ell & t_\ell^2 - r_\ell^2 \end{pmatrix} \tag{5.25}$$

Note that this matrix describes a non-invariant beam, i.e., the response from the opposite side of the interface is different. The overall matrix becomes

$$\mathbf{A} = \mathbf{F}\mathbf{L}_F\mathbf{I}_{1,3}\mathbf{L}_3\mathbf{I}_{3,4} \tag{5.26}$$

In this the matrices $\mathbf{I}_{n,m}$ and $\mathbf{L}_m$ are the normal Abelés matrices. The layer matrix $\mathbf{L}_F$, identical to the layer matrices $\mathbf{L}_m$ used in the Abelés formalism, has a phase factor $\Delta = h\omega n_0 cos\theta_0$, where h is the height of the excess dipoles above the Fresnel interface. If the particles are directly on the substrate surface, $h = d$.

The effect on the evaluated optical response of the TIF compared to Bruggeman's effective medium theory and MGT is illustrated in Fig. 20. This displays the measured value of the ellipsometric phase for a Si substrate covered with Au nanocolloids with 13.6 nm diameter. SEM measurements showed a surface coverage of 12%. With this surface coverage, the result of Bruggeman's EMA, the MGT result and the TIF result were calculated. Only the TIF result provides an accurate representation of the plasmon resonance observed around 2.25 eV. Bruggeman's EMA predicts a larger red shift of the resonance energy, whereas MGT has a correct resonance energy but a much smaller change in ellipsometric phase. A detailed analysis shows that the latter is a direct consequence of the optical coupling between the excess polarizability and the substrate properties as taken into account with the Abelés formalism [130]. The TIF theory has been successfully applied to ellipsometric studies of colloidal gold films [120,121,180–182] and colloidal crystals [119], as well as combined in situ surface difference reflection spectroscopy and GISAXS studies of the growth of silver island films Lazzari [183,184]. With the GISAXS parameters the model parameters in the TIF theory can be independently verified, showing excellent agreement with the calculations.

6. Plasmonic metamaterials

In the last decade, artificially structured materials with fascinating optical properties have been engineered. These "metamaterials" are composed of artificial "meta-atoms" – sub-wavelength metallic structures of dimension a, usually arranged in a periodic array of unit cell P. The simplest metamaterials may be defined as the nanoparticle composites and films described in Section 5. For those materials we used the concept of an effective medium and assigned an effective permittivity ε_{eff} to a bulk material composed of metal nanoparticles of radius a. The limiting requirement was that the dimensions of the particles were much less than the photon vacuum wavelength, $a \ll \lambda_0$. In principle, the same concept applies for an effective permeability μ_{eff}, however natural materials with a non-unity permeability at frequencies above the microwave regime are extremely rare.

In their seminal paper on "magnetism from conductors" [185] Pendry et al. proposed artificial metallic atoms in the form of dual, concentric, split-ring resonators (SRR). A magnetic field perpendicular to the axis of the ring induces a current around it (an inductive element) and the split in the ring, and also the gap between the two rings, act as a capacitive elements. Thus, the ring is analogous to an LC circuit and there will be a magnetic resonance with a Lorentzian dispersion

$$\mu_{\mathit{eff}}(\omega) = 1 + \frac{\omega_{\mathit{mp}}^2}{\omega_0^2 - \omega^2 - \mathrm{i}\Gamma\omega} \tag{6.1}$$

where the magnetic plasma frequency ω_{mp} and the resonance frequency ω_0 depend on the geometry of the rings and the conductivity of the metal [185]. Immediately above the resonance frequency the real part of μ_{eff} is negative (provided the impedance of the metal is low). While the idea of artificial magnetism was in itself novel, what garnered attention was the suggestion of creating a material with a negative refractive index by combining a negative μ with a negative ε (an idea theoretically proposed by Veselago in 1968 [186]), and the promise of a "perfect" lens [187]. Experimental demonstration of such a metamaterial in the microwave range soon followed by combining SRRs (negative μ_{eff}) with a wire array medium (negative ε_{eff}) [188].

Metamaterials have now become synonymous with negative refractive index materials (NIMs), and the field has progressed from the "double negative" materials described above, to negative refraction based on strong anisotropy, spatial dispersion and other phenomena. Thus one should distinguish between NIMs and materials (including metamaterials) which cause negative refraction due to other physical properties. The general condition for a NIM is often defined as that the angle between the wave vector $\mathbf{k}$ (in the direction of the phase velocity $\mathbf{v}_{\text{p}}$) and the Poynting vector $\mathbf{S}$ (in the direction of the group velocity $\mathbf{v}_{\text{g}}$) form an obtuse angle in the material, i.e., $\mathbf{k} \cdot \mathbf{S} < 0$. There are a number of contemporary books on metamaterials which cover this rapidly expanding field [189–191]. If metamaterials are to be applied as homogeneous materials in technological applications it is imperative that a procedure is defined by which the macroscopic material parameters may be determined. This in turn depends on defining an accepted mathematical description of metamaterials. Here we will discuss

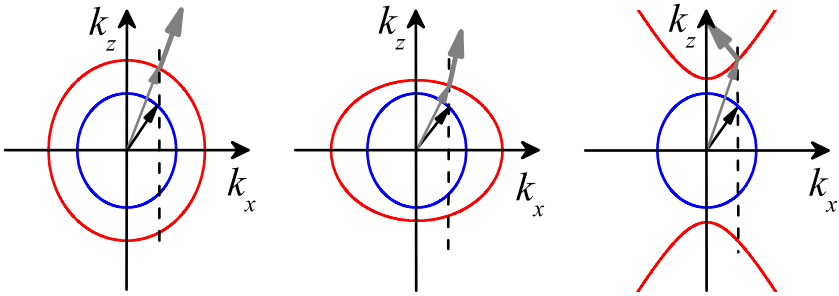

Fig. 21. The blue circles shows the isofrequency curves in air. For a given incident wave vector (black arrow) the refracted wave vector (thin grey arrow) in an isotropic material (a) will be parallel to the Poynting vector (thick grey arrow). In a weakly anisotropic material (b) they will not be parallel, and in a highly anisotropic indefinite material (c) the *x*-components will be anti-parallel. (For interpretation of the references to colour in this figure legend, the reader is referred to the web version of this article.)

three schemes by which negative refraction may be obtained and show that ellipsometry is well suited to the characterization of such materials, although significant challenges remain.

6.1. Highly anisotropic metamaterials

Negative refraction can occur at the interface of two non-magnetic media if the permittivity of one medium is highly anisotropic. This has been experimentally demonstrated in a natural anisotropic crystal such as YVO_4 [192], and in an artificially constructed super-lattice [193] and wire array composites [194]. In natural crystals the dielectric tensor elements are all positive and negative refraction occurs at a twinning plane in uniaxial crystals [192]. In artificially constructed non-magnetic *indefinite* metamaterials [195], one of the effective permittivity tensor elements is of opposite sign over a specified wavelength interval, and negative refraction may be observed in this range. Note that these are not NIMs since $\mathbf{k} \cdot \mathbf{S} > 0$.

Consider a plane-wave incident on an air-material interface in the x-z plane. The dispersion relation for an anisotropic material is

$$\frac{k_z^2}{\varepsilon_z} + \frac{k_x^2}{\varepsilon_x} = \frac{\omega^2}{c^2} \tag{6.2}$$

The direction of the group and phase velocities are observed in a plot of the isofrequency curves in *k*-space (Fig. 21). For a given point on the isofrequency curve the wave vector **k** (thin arrow) is represented by a vector from the origin to that point, and the Poynting vector **S** (thick arrow) is normal to the tangent to the curve at that point. If the material is isotropic the isofrequency curve will be circular (Fig. 21(a)), and **k** and **S** will be parallel in all directions. In weakly anisotropic materials the isofrequency curve will describe an ellipse (Fig. 21(b)) and the group and phase velocities are in general not parallel. For highly anisotropic indefinite materials (e.g., with $\varepsilon_x > 0$ and $\varepsilon_z < 0$) the isofrequency curve is hyperbolic (Fig. 21(c)) and the signs of k_x and S_x are opposite, leading to negative refraction [196].

Using the above concepts, anisotropic wire arrays have been used to experimentally demonstrate negative refraction [194]. In many cases the Maxwell-Garnett effective medium theory with anisotropic screening parameters accurately predicts the permittivity of wire arrays [196]. However Belov et al. showed that a uniaxially anisotropic wire array does not show purely local dispersion but rather shows strong spatial dispersion even in the long wavelength limit [197]. Interestingly, isotropic sub-wavelength wire arrays were one of the first optical metamaterials, designed to provide control over the effective plasma frequency. The value of the plasma frequency defined in Eq. (3.4) is defined by the electron density, N_e, and the effective mass, m_e. We may assign an effective plasma frequency to a nanowire composite, with N_e proportional to the fill factor F of the metallic component.

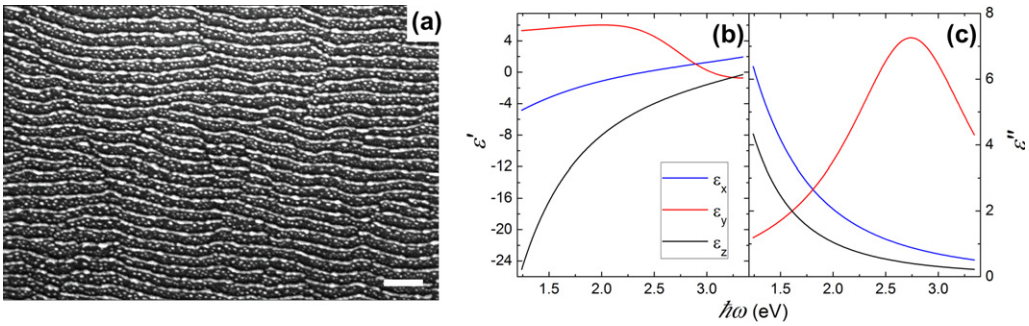

Fig. 22. (a) SEM image of silver nanowires deposited by oblique evaporation on ion-sputtered rippled substrates (scale bar = 100 nm). (b) and (c) show the effective dielectric tensor elements for the three orthogonal directions determined using generalized ellipsometry. The blue line (*x*-direction) and red line (*y*-direction) are horizontal and vertical in the plane of the page, respectively. The black line (*z*-direction) is normal to the page. (adapted from [200]). (For interpretation of the references to colour in this figure legend, the reader is referred to the web version of this article.)

In a sub-wavelength wire arrays we must also take into account the self-inductance of the wires which significantly increases m_e. Pendry et al. showed that the plasma frequency could be pushed into the far-infrared using isotropic 3D wire arrays [198].

To characterize anisotropic wire arrays requires the determination of the three orthogonal permittivity tensor components. In a 3D array of oriented, equally-spaced nanowires two of the tensor elements are degenerate, resulting in a uniaxially anisotropic material. In an ellipsometry measurement, if the long axis of the wires is oriented perpendicular to the substrate surface, as in [194], then $\varepsilon_x = \varepsilon_y \neq \varepsilon_z$ and the ordinary (ε_x, ε_y) and extra-ordinary (ε_z) tensor components may be determined using standard ellipsometry with measurements at multiple incident angles. If the long axis of the wires is parallel to the substrate surface, or otherwise inclined at an angle, then $\varepsilon_x \neq \varepsilon_y \neq \varepsilon_z$ and the optical properties should be determined using generalized ellipsometry (Section 2.2.3).

As an example we consider a single layer of aligned metallic wires which is biaxially anisotropic (i.e., $\varepsilon_x \neq \varepsilon_y \neq \varepsilon_z$). Sub-wavelength 2D wire arrays were produced by evaporating metal at an oblique angle onto self-organized periodic ripple patterns formed by low-energy ion beam sputtering [199]. Fig. 22 shows SEM micrographs of these silver wires formed on a 35 nm period silicon ripple pattern. The dielectric tensor components of these arrays were determined using generalized ellipsometry [200]. In the direction parallel to the wires the tensor component exhibits a predominantly metallic behaviour. However perpendicular to the wires a large plasmon resonance is observed with the real part being positive at frequencies below the resonance frequency. In the direction perpendicular to the surface the tensor component is close to the bulk silver dielectric function. A plane wave in the x-y or y-z planes would be expected to show negative refraction at frequencies below the resonance ($\varepsilon_y > 0$). There will be an optimum frequency and direction where the losses are minimized. If the wires are discontinuous (arrays of aligned rods of spheres) then the plasmon resonances are observed in both ε_x and ε_y, with different resonance frequencies depending primarily on the surface coverage of the silver in that direction. The range of negative refraction is thus tuneable [201], however the high absorption near the resonances severely limits such a scheme.

Super-lattices – alternating layers of selectively doped semiconductors or metal/dielectrics – display resonant behaviour. As shown in Section 3.6, a single layer of silver has a resonant LO mode at the screened plasma frequency. A multilayer stack of these layers, separated by a dielectric may be described by an effective medium expression with a depolarization factor L (Eq. (5.14)) equal to 1 (maximum screening) in the direction perpendicular to the layer plane. The effective dielectric function in this direction will exhibit a resonance, with the frequency dependent on the volume fraction of the layers and the dielectric functions of the materials. Humlicek presented an ellipsometric investigation of a super-lattice of doped semiconductors, with the resonance located in the infrared [202], and reproduced the measured parameters with an effective medium approach. These same materials were demonstrated to show negative refraction [193].

6.2. Metamaterials with artificial effective permeability

Materials which have simultaneous negative effective permittivity and permeability have a negative refractive index and are true NIMs ($\mathbf{k}\cdot\mathbf{S}<0$). The unambiguous retrieval of ε_{eff} and μ_{eff} from metamaterials is not a trivial task. Additionally, mathematically describing these materials using ε_{eff} and μ_{eff} is only one way to define the macroscopic material parameters. An alternative description based on spatial dispersion is essentially equivalent for materials in the optical range.

6.2.1. Parameter retrieval

The study of metamaterials originated in microwave research [203] where it is relatively straightforward to fabricate sub-wavelength artificial atoms, and much of the terminology is derived from that field. Smith et al. [204] discussed the inverse problem of retrieving the constitutive parameters ε_{eff} and μ_{eff} of metamaterials from transmission and reflection coefficients (which are also referred to as scattering parameters in microwave research, and hence the method is termed S-parameter retrieval). The S-parameter method was developed to determine the complex refractive index $N=\sqrt{\varepsilon\mu}$ and impedance $Z=\sqrt{\mu/\varepsilon}$ of a thin film of thickness d from the complex transmission coefficient t and reflection coefficient r, given by

$$Z=\pm\left[\frac{(1+r)^2-t^2}{(1-r)^2-t^2}\right]^{\frac{1}{2}} \tag{6.3a}$$

and

$$\cos(Nkd)=\frac{(1-r)^2+t^2}{2t} \tag{6.3b}$$

where k is the free-space wave vector. Clearly this method does not give unique solutions for complex ε and μ although it is possible to resolve the issue by a process of intuitive elimination [189]. Importantly, normal incidence reflection and transmission measurements contain no magnetic field component perpendicular to the surface, and thus a magnetic resonance cannot be directly excited by the magnetic field component in planar SRRs under normal incidence. In an important step for ellipsometry applications, Eq. (6.3) have since been extended for oblique incidence reflection and transmission [205].

As micro-fabrication methods pushed metamaterials further toward the optical range ellipsometry was identified as an important characterization method. In 2004 Yen et al. used ellipsometry to demonstrate a terahertz magnetic response in 3 different sized SRRs with dimensions from 2 to 50 μm [206]. Ellipsometric parameters were measured at 30° incidence angle, over the frequency range from 0.6 – 1.8 THz. The authors chose to represent the data as the absolute inverse square of $\rho(\omega)$. They argue that this parameter is the natural function to use because it provides the ratio of the magnetic to electric response from the SRRs. However the phase information was ignored, and parameter retrieval was not attempted.

The retrieval problem is essentially one of measuring more independent experimental parameters than the unknowns in the equations. This in turn depends on the symmetry properties of the material. The ellipsometric parameters Ψ and Δ are sufficient to determine complex ε for isotropic, non-magnetic materials if the thickness is known. If the material is uniaxially anisotropic then multiple incident angle measurements may be sufficient to determine the 4 unknowns, depending on the sample orientation. If the material is biaxially anisotropic then generalized ellipsometry (GE) provides the 6 unknowns required to determine the solution. Marques et al. [207] showed that SRRs are bi-anisotropic, i.e., they have magneto-electric coupling. In addition to the 2nd-rank tensors $\overline{\overline{\varepsilon}}$ and $\overline{\overline{\mu}}$, the magneto-optical permittivities, $\overline{\overline{\xi}}$ and $\overline{\overline{\zeta}}$ – which describe the coupling of the magnetic-to-electric response and electric-to-magnetic response, respectively – must also be defined (these are also called the gyrotropic parameters).

$$\mathbf{D}=\varepsilon_0\overline{\overline{\varepsilon}}\mathbf{E}+\left(\overline{\overline{\xi}}/c\right)\mathbf{H} \tag{6.4a}$$

Table 6.1
The material parameters that influence the polarized reflection coefficients for orthogonal planes of incidence.

	x–*z* plane	*y*–*z* plane	*x*–*y*–*z* plane
r_p	ε_x, μ_y, ε_z	μ_x, ε_y, ε_z	ε_x, ε_y, ε_z, μ_x, μ_y
r_s	μ_x, ε_y, μ_z	ε_x, μ_y, μ_z	ε_x, ε_y, μ_x, μ_y, μ_z

$$\mathbf{B} = \mu_0\overline{\overline{\mu}}\mathbf{H} + \left(\overline{\overline{\zeta}}/c\right)\mathbf{E} \tag{6.4b}$$

Thus to describe the complete electromagnetic properties of SRRs one needs four 2nd rank tensors – potentially up to 36 complex quantities.

In practice, the gyrotropic parameters are often vanishingly small and then one normally needs to determine only the diagonal elements of $\overline{\overline{\varepsilon}}$ and $\overline{\overline{\mu}}$. The 6 parameters determined from generalized ellipsometry (GE) are therefore not sufficient to unambiguously determine these 6 complex parameters. The sample orientation with respect to the plane of incidence is of critical importance in determining how the anisotropy influences the measurement. Table 6.1 shows the material parameters that influence the polarized reflection coefficients for orthogonal planes of incidence. An ellipsometric measurement in just one plane parallel to the optical axis will be influenced by all the orthogonal tensor elements, however only two independent parameters will be measured. GE measurements at multiple incidence, rotation and polarization angles should allow one to over-determine the system.

For parameter retrieval the refractive index in the Fresnel equations (Eqs. (2.13) and (2.14)) may be defined by the four tensors in Eq. (6.4), rather than the straightforward dependence on ε. A derivation for the Fresnel coefficients for a bianisotropic materials is given in [190]. The most general description for oblique coherent reflection for an anisotropic material is Berreman's 4×4 matrix formalism [41]. With the Berreman formalism one can analytically model the dependence of the transmission and reflection Fresnel coefficients and derive in first order their analytic dependence on the effective permeability and permittivity tensor components. The forward problem of calculating the ellipsometric response from pre-defined material parameters has recently been performed using the Berreman formalism [208]. The retrieval of the material parameters from measured ellipsometric data by mathematical inversion has to date not been reported for artificial magnetic metamaterials. However ellipsometry is still extremely useful for characterizing NIMs, as we will show below.

6.2.2. Characterisation of single split ring resonators

After the initial demonstration of artificial magnetism in SRRs at microwave frequencies there was steady progress toward the THz range by a process of miniaturization [206]. A surprising advance was reported by Linden et al. [209] who claimed to observe a magnetic response at 100 THz (3 μm) in single split-ring resonators (SSRR) (Fig. 23), even when the magnetic field is parallel to the plane of the SSRR. In this geometry the magnetic field will not generate a current in the ring, and hence no magnetic response was expected. However, using only polarised light at near-normal incidence, the authors showed that a magnetic-type resonance could still be observed. The explanation is that an electric field polarized in the *x* direction (Fig. 23) will initiate a current in the ring which is out-of-phase in the two *y*-arms, thus creating a magnetic moment. The plasmon resonances established in the arms will thus couple asymmetrically [210]. Conversely, with the electric field in the *y*-direction, the currents in the arms will be in-phase, the plasmon resonances will couple symmetrically and no magnetic moment will be established. The SSRR structure has since been pushed to the limits of microfabrication, exhibiting magnetic resonances at above 300 THz (900 nm) [211].

SSRRs have been investigated by IR-ellipsometry [212]. Periodically arranged gold SSRRs on a Si substrate (native oxide) were fabricated using nano-imprint lithography with dimensions of $P = 1000$ nm, base and side legs = 780 nm, width = 80 nm, gap = 250 nm, and gold layer thickness $d = 54$ nm on a 2 nm layer of Ti. The ellipsometric spectra were measured using FTIR spectroscopic ellipsometry at AOI = 45° and 65° in the *xz* and *yz* incidence planes. The ellipsometric angles are shown in Fig. 23. Pronounced peaks are observed in the Ψ spectra in the *xz*-plane at 800 cm^{-1} and 2200 cm^{-1}. These correspond to the first and third (i.e., asymmetrically coupled) plasmonic modes of the SSRR. In

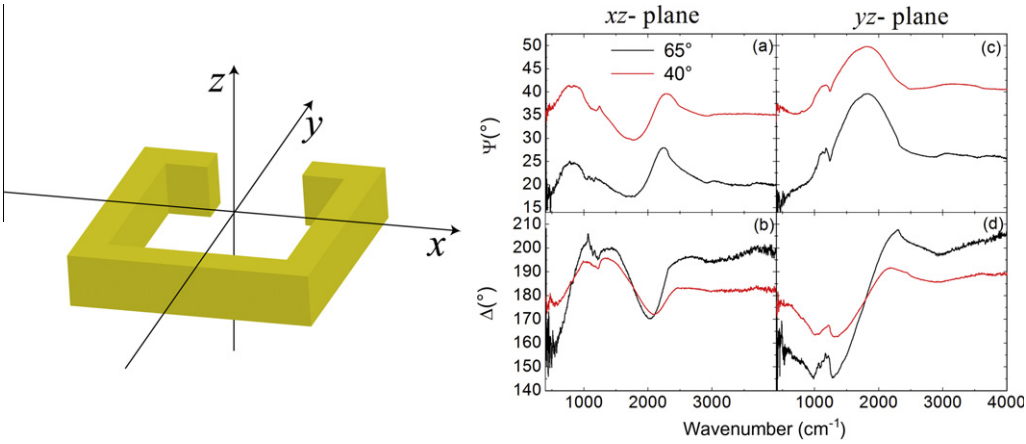

Fig. 23. Left, a SSRR showing the measurement co-ordinates. On the right are ellipsometric angles of an array of SSRRs (dimensions in text) measured at 40° and 65° in the *xz*- and *yz*-planes.

the *yz*-plane a pronounced peak at 1700 cm^{-1} and a weak peak at 2900 cm^{-1}, corresponding to the second and fourth plasmonic modes [213] are observed. The peaks in Ψ correspond primarily to the peaks in r_p. Similarly the phase difference Δ is also dominated by the p-polarised phase response. Note that unambiguous retrieval of the tensor elements of ε_{eff} and μ_{eff} is not possible from these measurements alone, and the gyrotropic parameters may also be present [214].

6.2.3. Characterisation of fishnet metamaterials

In recent years a range of new designs with improved symmetry have emerged. Most of these are based on a simple design of pairs of rods. Podolskiy [215] theorised that metallic rod pairs may exhibit a diamagnetic response and negative index in the optical range due to a localized plasmonic resonance. As with the SSRR design, opposing currents in the lengths of the rods produce an effective magnetic moment. The main difference to the SSRRs is that the driving mechanism is the phase difference in the plane wave, and not the current in the base arm of the ring. In 2005, Shalaev demonstrated this experimentally with magnetic resonances near the important communications wavelength of 1.5 μm [216]. The Babinet principle indicates that if pairs of conductive rods in a dielectric medium exhibit magnetic resonances, then elongated holes in parallel metallic films should also be magnetically active. This is the basis for the resonant structures demonstrated by Zhang et al., first using circular holes [217] and later using elliptical holes [218]. This idea was taken further by the same group in a "nano fishnet" structure of rectangular holes in parallel metallic films (Fig. 24). They achieved a real refractive index of −2 at a wavelength of 1.45 μm [219], and later a value of $n = -0.6$ at 780 nm [220].

A fishnet metamaterial produced by nanoimprint lithography was recently investigated by spectroscopic ellipsometry [221]. The fishnet material comprises a three layer structure of Au/MgO/Au (each 30 nm) on a glass substrate with periodic rectangular holes (Fig. 24). The hole dimensions are 135 x 350 nm, and the unit cell is 500 x 600 nm in the x- and y-directions, respectively. The sidewall angles, due to the fabrication procedure, are 20°. Ellipsometric data was taken in two orthogonal directions along the *xz*- and *yz*- planes of the material, using Vis-NIR ellipsometry (Fig. 24(a-d)). In the *xz*- plane the large angle dependent resonance peaks below 1100 nm are due to diffraction effects (the Wood/Rayleigh anomaly). The intense peaks near 1300 nm corresponds to the symmetrically coupled plasmon resonances in the gold layers. The small resonance at higher wavelengths is the anti-symmetric resonance, designed to provide a negative μ_{eff} (the continuous gold strips provide ε_{eff}). The resonance frequency is above 2000 nm and dependent on the incidence angle in the *xz*-plane, however it is near 1800 nm and independent on the AOI in the *yz*-plane. Similarly to the SSRRs, these standard ellipsometric measurements do not provide enough information to unambiguously

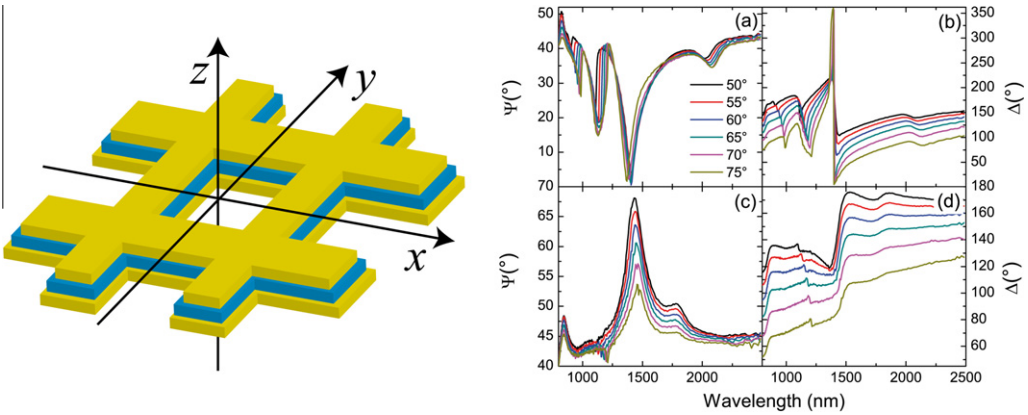

Fig. 24. Left, schematic of a three layer fishnet material, and right, measured ellipsometric parameters in the *xz*- (a, b) and *yz*-planes (c, d).

determine the optical tensor elements, however the rational to assign homogenized parameters to these materials is debatable, discussed below.

6.2.4. Spatial dispersion

The SSRRs and fishnet designs rely on coupled localized plasmon resonances in adjacent metallic rods or plates. The magnetic resonance corresponds to an anti-symmetric coupling. The separation of the rods must be optimized: they must be close enough that the coupling splits the isolated plasmon resonance into a blue shifted symmetric mode and a red-shifted anti-symmetric mode, but separated by enough that the anti-symmetric mode is not over-damped [210]. The required separation brings into question the validity of the long wavelength assumption and the homogenization of the effective parameters. Essentially, the origin of the magnetic resonance depends on spatial dispersion, i.e., the anti-symmetric coupling *requires* a non-local electric field in the medium. This can be observed in the fact that the dimensions of the SSRR and fishnet metamaterials are generally larger than $\lambda_0/10$.

Describing metamaterials using an effective permeability has been heavily debated. At issue is the use of a magnetic description at frequencies where magnetism loses its physical meaning. In fact the plasmonic resonances are caused by currents initiated by the electric field component of the light. An alternative method of describing materials with *weak* spatial dispersion is to expand in a power series the generalized dielectric tensor $\varepsilon_{ij}(\omega,\mathbf{k})$ up to second order in the wave vector, k such that [222]

$$\varepsilon_{ij}(\omega,\mathbf{k}) = \varepsilon_{ij}(\omega) + \mathrm{i}\gamma_{ijl}(\omega)k_l + \alpha_{ijlm}(\omega)k_l k_m \tag{6.5}$$

where $\varepsilon_{ij}(\omega)$ is the usual dielectric tensor and $\gamma_{ijl}(\omega)$ and $\alpha_{ijlm}(\omega)$ are tensors which include spatial dispersion of first and second order, respectively. In a material with spatial inversion symmetry the second term (representing the gyrotropic or chiral response) vanishes. The third term is associated with the magnetic dipole response but also contains information about the electric quadrupole [223]. Note that the effective permeability description and the weak spatial dispersion description are mathematically equivalent. Menzel et al. [205] have derived the incident angle dependent forms of eqs (6.2) and (6.3) in terms of the incident wave vector. By applying the equations to a fishnet metamaterial they conclude that the retrieved parameters N and Z strongly depend on the lateral wave vector component (i.e., the incident angle). They also showed that the long-wavelength assumption implicit in applying an $\varepsilon_{\mathrm{eff}}$ and μ_{eff} to metamaterials is generally violated [205]. Thus there is still debate over whether it is appropriate to describe materials with a magnetic resonance based on anti-symmetrically coupled plasmon resonances using homogenized effective material parameters. One should always consider that metamaterials occur in the interesting range between a purely homogeneous material and a non-local medium such as a photonic crystal.

6.3. Chiral metamaterials

An alternative route to negative refraction using chiral materials was theoretically predicted independently by Pendry [224]and Tretyakov et al. [225]. In a chiral material the asymmetry defines the magneto-optical parameters in (Eq. (6.4)) as $\xi = -\zeta$. The refractive index is defined for a chiral material as $N_{L,R} = \sqrt{\varepsilon\mu} \pm \xi$ where the subscripts L and R denote left and right circularly polarized light respectively. Thus in a metamaterial where ε and μ are simultaneously small and ξ is large enough to dominate, one of the circular polarization states may exhibit a negative N.

In transmission, Mueller matrix ellipsometry (or polarimetry) is the method of choice for characterization of chiral materials [226]. Similarly, reflection ellipsometry has been applied for over a decade to the study of chiral materials such as liquid crystals [43] [227]. Chirality is observed in transmission mode as non-zero contributions to the off-diagonal Mueller matrix elements. However the off-diagonal MM elements are convolutions of contributions from linear and circular birefringence and dichroism. It is possible to decompose the measured MM into products representing basic optical devices [228]. In reflection mode it is crucial to distinguish between linear birefringence due to anisotropy, and chiral effects due to intrinsic gyrotropy.

It is interesting to note that chiral metamaterials consisting of nanoscale coils fabricated by glancing angle deposition were proposed in the early 1990s [229], well before the recent interest in negative index metamaterials. Such materials were recently fabricated and characterised by ellipsometry [230]. Another class of materials often classified as metamaterials is sub-wavelength hole arrays (SWHA) in metal films. Ebbesen et al. showed in 1998 that the measured transmission through an optically thick silver film perforated with a SWHA was higher than expected by the theory of Bethe [231]. The observation has been explained by considering the coupling of the light to surface plasmon polaritons which guide the energy through the holes [232].

Due to spatial dispersion, the study of SWHAs by ellipsometry is not straightforward. However with the advent of fully automated angle of incidence, rotation angle and data collection, combined with the necessary data processing, ellipsometry appears set to contribute to the study of SWHAs, especially in the Mueller matrix configuration. Braun et al. used MME to measure the reflection properties of SWHAs on very thin gold layers [233]. The data is represented by polar contour plots (incident and rotation angles) of the MM elements at a specific frequency. This allows one to interpret the rotational symmetry of the scattered orders. Gompf et al. [234] showed that using MM ellipsometry one can observe chiral effects such as optical activity and circular dichroism in SWHAs. The authors point out that these effects arise not from any inherent magnetism, but from spatial dispersion.

7. Outlook

The utility of spectroscopic ellipsometry is only beginning to be discovered for the characterization of plasmonic thin films and metamaterials. New advances in ellipsometric hardware and software continue to create opportunities to study complex nanostructured materials, while at the same time the range of materials is expanding dramatically due to new fabrication techniques. This review gives a summary of the state-of-art with the additional aim of providing a coherent terminology to describe new materials and systems.

The scope for combining ellipsometry in sensing applications using TIRE is vast, both for biological and gas sensing. The increase in the speed of data acquisition, combined with in situ ellipsometry measurement geometries will be a rapidly growing field for the study of the growth of metal island films and their interaction with gases and organic molecules. Sculpting these films using oblique-angle incidence and ion-beam sputtering will result in the creation of anisotropic particles and distributions which will have unusual optical properties. The symmetric and anti-symmetric coupling of plasmonic resonances in such materials, and others designed and manufactured using top-down-methods, will providing a fertile and challenging field for ellipsometric characterization of chiral materials and effects based on weak spatial dispersion. The further development of effective medium and thin island film theories, and a coherent description of spatial dispersion in metamaterials, are required to provide accurate homogenized optical parameters to these complex materials.

Acknowledgements

We wish to thank Karsten Hinrichs, Bruno Gompf, Mathias Schubert, Babak Dastmalchi, Kurt Hingerl, Iris Bergmair, Milka Jakovljevic for fruitful discussions. Financial support from the EU FP7 project NIMNIL is also acknowledged.

Appendix A

The dipolar and quadrupole depolarization factors as a function of surface coverage are:

$$L_{\mathrm{p}} = \frac{1}{3}\left[1 - \frac{\phi}{2} + B_{\mathrm{sa}}\left(\frac{1}{8} - \frac{\phi}{4\sqrt{2}}\right)\right]$$

$$L_z = \frac{1}{3}\left[1 + \phi + B_{\mathrm{sa}}\left(\frac{1}{4} - \frac{\phi}{2\sqrt{2}}\right)\right]$$

$$L1_{\mathrm{p}} = \frac{2}{5}\left[1 - \frac{\phi}{8} + \frac{B_{\mathrm{sa}}}{8}\left(1 - \phi\left(\frac{1}{\sqrt{2}}\frac{3}{8}\right)\right)\right]$$

$$L1_z = \frac{2}{5}\left[1 + \frac{3\phi}{16} + \frac{3B_{\mathrm{sa}}}{16}\left(1 - \phi\left(\frac{1}{\sqrt{2}}\frac{3}{8}\right)\right)\right]$$

$$\Lambda_{\mathrm{p}} = -\frac{B_{\mathrm{sa}}^2}{640}\left(-1 + \frac{\phi}{\sqrt{2}}\right)^2$$

$$\Lambda_z = -\frac{3B_{\mathrm{sa}}^2}{640}\left(-1 + \frac{\phi}{\sqrt{2}}\right)^2$$

The image effect is incorporated in these depolarization factors by an attenuation factor $B_{\mathrm{sa}} = (\varepsilon_{\mathrm{a}} - \varepsilon_{\mathrm{s}})/(\varepsilon_{\mathrm{a}} + \varepsilon_{\mathrm{s}})$ that descibes the contrast between ambient and substrate. This contrast is quite considerable for semiconductors and metals ($B_{\mathrm{sa}} \approx -1$), whereas it is quite reduced for dielectrics. For instance for a glass substrate in a water ambient, B_{sa} and thus the image effect, is reduced by an order of magnitude compared to metals. Note that as a result of the image effect the sum of the depolarization factors $L_{\mathrm{p}} + L_z = 1 + \frac{B_{\mathrm{sa}}}{3}\left(\frac{1}{2} - \frac{\phi}{\sqrt{2}}\right)$ no longer equals 1.

References

[1] M. Faraday, Experimental relations of gold (and other metals) to light, Philosophical Transactions of the Royal Society of London 147 (1857) 145.
[2] I. Freestone, N. Meeks, M. Sax, C. Higgitt, The Lycurgus cup – a Roman nanotechnology, Gold Bulletin 40 (2007) 270–277.
[3] H.A. Atwater, S. Maier, A. Polman, J.A. Dionne, L. Sweatlock, The new "p-n junction". Plasmonics enables photonic access to the nanoworld, MRS Bulletin 30 (2005) 385–389.
[4] S.A. Maier, Plasmonics: Fundamentals and Applications, Springer, 2007.
[5] K. Kneipp, Y. Wang, H. Kneipp, L.T. Perelman, I. Itzkan, R. Dasari, M.S. Feld, Single molecule detection using surface-enhanced Raman scattering (SERS), Physical Review Letters 78 (1997) 1667–1670.
[6] H.A. Atwater, A. Polman, Plasmonics for improved photovoltaic devices, Nature Materials 9 (2010) 10.
[7] K. Okamoto, I. Niki, A. Shvartser, Y. Narukawa, T. Mukai, A. Scherer, Surface-plasmon-enhanced light emitters based on InGaN quantum wells, Nature Materials 3 (2004) 601–605.
[8] J. Homola, S.S. Yee, G. Gauglitz, Surface plasmon resonance sensors: review, Sensors and Actuators B – Chemical 54 (1999) 3–15.
[9] J.B. Pendry, D. Schurig, D.R. Smith, Controlling electromagnetic fields, Science 312 (2006) 1780–1782.
[10] M. Losurdo, M. Bergmair, G. Bruno, D. Cattelan, C. Cobet, A. de Martino, K. Fleischer, Z. Dohcevic-Mitrovic, N. Esser, M. Galliet, R. Gajic, D. Hemzal, K. Hingerl, J. Humlicek, R. Ossikovski, Z.V. Popovic, O. Saxl, Spectroscopic ellipsometry and polarimetry for materials and systems analysis at the nanometer scale: state-of-the-art, potential, and perspectives, Journal of Nanoparticle Research 11 (2009) 1521–1554.
[11] P. Drude, Optical properties and electron theory, Ann. Phys.-Berlin 14 (1904) 677–725.
[12] P. Drude, Optical properties and the electron theory, Ann. Phys.-Berlin 14 (1904) 936–961.

[13] P. Drude, The electron theory of metals, Ann. Phys.-Berlin 7 (1902) 687–692.
[14] P. Drude, On the electron theory of metals, Ann. Phys.-Berlin 1 (1900) 566–613.
[15] A.C. Hall, A century of ellipsometry, Surface Science 16 (1969) 1.
[16] R.W. Wood, A suspected case of the electrical resonance of minute metal particles for light-waves. A new type of absorption, Philosophical Magazine 3 (1902) 396–410.
[17] R.M.A. Azzam, Ellipsometry, in: M. Bass (Ed.), Handbook of Optics, McGraw-Hill, London, 2010.
[18] R.M.A. Azzam, N.M. Bashara, Ellipsometry and Polarized Light, Elsevier, 1987.
[19] H. Fujiwara, Spectroscopic Ellipsometry: Principles and Applications, Wiley, West Sussex, 2007.
[20] M. Schubert, Infrared ellipsometry on semiconductor layer structures – phonons, plasmons, and polaritons, Springer Verlag, Berlin, 2004.
[21] H.G. Tompkins, E.A. Irene, Handbook of Ellipsometry, William Andrew - Springer, Norwich/Heidelberg, 2005.
[22] M. Born, E. Wolf, Principles of Optics, 7th ed., Cambridge University Press, Cambridge, 1999.
[23] L.D. Landau, L.P. Lifshitz, Electrodynamics of Continuous Media, 2nd ed., Pergamon Press, 1984.
[24] J. Humlicek, Polarized Light and Ellipsometry, in: H.G. Tompkins, E.A. Irene (Eds.) Handbook of Ellipsometry, William Andrew - Springer, Norwich/Heidelberg, 2005.
[25] M. Dressel, B. Gompf, D. Faltermeier, A.K. Tripathi, J. Pflaum, M. Schubert, Kramers–Kronig-consistent optical functions of anisotropic crystals: generalized spectroscopic ellipsometry on pentacene, Optics Express 16 (2008) 19770–19778.
[26] E. Hecht, Optik, 17th ed., Oldenbourg, München, 2009.
[27] D.E. Aspnes, Expanding horizons: new developments in ellipsometry and polarimetry, Thin Solid Films 455 (2004) 3–13.
[28] J. Lee, R.W. Collins, Real-time characterization of film growth on transparent substrates by rotating-compensator multichannel ellipsometry, Applied Optics 37 (1998) 4230–4238.
[29] U. Richter, Application of the degree of polarization to film thickness gradients, Thin Solid Films 313 (1998) 102–107.
[30] K.H. Jun, J.H. Kwak, K.S. Lim, Simulation of depolarization effect by a rough surface for spectroscopic ellipsometry, Journal of the Optical Society of America. A, Optics, Image Science, and Vision 20 (2003) 1060–1066.
[31] W.A. Shurcliff, Polarized Light: Production and Use, Harvard University Press, Cambridge, MA, 1962.
[32] G.E. Jellison, Data-Analysis for Spectroscopic Ellipsometry, Thin Solid Films 234 (1993) 416–422.
[33] R.M.A. Azzam, N.M. Bashara, Generalized Ellipsometry for Surfaces with Directional Preference – Application to Diffraction Gratings, Journal of the Optical Society of America 62 (1972) 1521–1523.
[34] M. Schubert, Theory and application of generalized ellipsometry, in: H.G. Tompkins, E.A. Irene (Eds.), Handbook of Ellipsometry, William Andrew – Springer, Norwich/Heidelberg, 2005.
[35] C.F. Bohren, D.R. Huffman, Absorption and Scattering of Light by Small Particles, John Wiley Sons, Weinheim, 1983
[36] F. Abeles, Optical-Properties of Very Thin-Films, Thin Solid Films 34 (1976) 291–302.
[37] F. Abeles, La theorie generale des couches minces, Journal De Physique Et Le Radium 11 (1950) 307–309.
[38] H. Arwin, D.E. Aspnes, Unambiguous determination of thickness and dielectric function of thin-films by spectroscopic ellipsometry, Thin Solid Films 113 (1984) 101–113.
[39] T.W.H. Oates, D.R. McKenzie, M.M.M. Bilek, Percolation threshold in ultrathin titanium films determined by in situ spectroscopic ellipsometry, Physical Review B 70 (2004) 195406.
[40] J.N. Hilfiker, N. Singh, T. Tiwald, D. Convey, S.M. Smith, J.H. Baker, H.G. Tompkins, Survey of methods to characterize thin absorbing films with spectroscopic ellipsometry, Thin Solid Films 516 (2008) 7979–7989.
[41] D.W. Berreman, Optics in stratified and anisotropic media – 4×4-matrix formulation, Journal of the Optical Society of America 62 (1972) 502–510.
[42] M. Schubert, B. Rheinlander, J.A. Woollam, B. Johs, C.M. Herzinger, Extension of rotating-analyzer ellipsometry to generalized ellipsometry: Determination of the dielectric function tensor from uniaxial TiO_2, Journal of the Optical Society of America. A, Optics, Image Science, and Vision 13 (1996) 875–883.
[43] M. Schubert, Generalized ellipsometry and complex optical systems, Thin Solid Films 313 (1998) 323–332.
[44] C. Kittel, Introduction to Solid State Physics, 7th ed., John Wiley Sons, New York, 1996.
[45] A. Vial, A.S. Grimault, D. Macias, D. Barchiesi, M.L. de la Chapelle, Improved analytical fit of gold dispersion: Application to the modeling of extinction spectra with a finite-difference time-domain method, Physical Review B 71 (2005) 085416.
[46] G.E. Jellison, F.A. Modine, Parameterization of the optical functions of amorphous materials in the interband region, Applied Physics Letters 69 (1996) 371–373.
[47] J. Tauc, Grigorov.R, A. Vancu, Optical properties and electronic structure of amorphous germanium, Physica Status Solidi 15 (1966) 627–637.
[48] A.R. Forouhi, I. Bloomer, Optical dispersion-relations for amorphous-semiconductors and amorphous dielectrics, Physical Review B 34 (1986) 7018–7026.
[49] H. Fujiwara, M. Kondo, Effects of carrier concentration on the dielectric function of ZnO: Ga and In_2O_3: Sn studied by spectroscopic ellipsometry: Analysis of free-carrier and band-edge absorption, Physical Review B 71 (2005) 075109.
[50] Y.J. Cho, N.V. Nguyen, C.A. Richter, J.R. Ehrstein, B.H. Lee, J.C. Lee, Spectroscopic ellipsometry characterization of high-k dielectric HfO2 thin films and the high-temperature annealing effects on their optical properties, Applied Physics Letters 80 (2002) 1249–1251.
[51] P.G. Etchegoin, E.C. Le Ru, M. Meyer, An analytic model for the optical properties of gold, Journal of Chemical Physics 125 (2006) 164705.
[52] D.W. Lynch, W.R. Hunter, in: E.D. Palik (Ed.), Handbook of Optical Constants of Solids, Academic Press, New York, 1985.
[53] P.B. Johnson, R.W. Christy, Optical-Constants of Noble-Metals, Physical Review B 6 (1972) 4370–4379.
[54] M.A. Ordal, R.J. Bell, R.W. Alexander, L.L. Long, M.R. Querry, Optical-properties of 14 metals in the infrared and far infrared - Al, Co, Cu, Au, Fe, Pb, Mo, Ni, Pd, Pt, Ag, Ti, V, and W, Applied Optics 24 (1985) 4493–4499.
[55] M.A. Ordal, L.L. Long, R.J. Bell, S.E. Bell, R.R. Bell, R.W. Alexander, C.A. Ward, Optical-properties of the metals Al, Co, Cu, Au, Fe, Pb, Ni, Pd, Pt, Ag, Ti, and W in the infrared and far infrared, Applied Optics 22 (1983) 1099–1119.
[56] T. Hollstein, U. Kreibig, F. Leis, Optical-properties of Cu and Ag in intermediate region between pure drude and interband absorption, Physica Status Solidi B – Basic Research 82 (1977) 545–556.

[57] K. Stahrenberg, T. Herrmann, K. Wilmers, N. Esser, W. Richter, M.J.G. Lee, Optical properties of copper silver in the energy range 2.5–9.0 eV, Physical Review B 64 (2001).
[58] NanoCHarM, in: http://www.nanocharm.org/.
[59] A.D. Rakic, A.B. Djurisic, J.M. Elazar, M.L. Majewski, Optical properties of metallic films for vertical-cavity optoelectronic devices, Applied Optics 37 (1998) 5271–5283.
[60] U. Kreibig, M. Vollmer, Optical Properties of Metal Clusters, Springer, Berlin, 1995.
[61] P.R. West, S. Ishii, G.V. Naik, N.K. Emani, V.M. Shalaev, A. Boltasseva, Searching for better plasmonic materials, Laser and Photonics Reviews 4 (2010) 795–808.
[62] C. Langhammer, M. Schwind, B. Kasemo, I. Zoric, Localized surface plasmon resonances in aluminum nanodisks, Nano Letters 8 (2008) 1461–1471.
[63] Y. Ekinci, H.H. Solak, J.F. Loffler, Plasmon resonances of aluminum nanoparticles and nanorods, Journal of Applied Physics 104 (2008) 083107.
[64] P.C. Wu, C.G. Khoury, T.H. Kim, Y. Yang, M. Losurdo, G.V. Bianco, T. Vo-Dinh, A.S. Brown, H.O. Everitt, Demonstration of surface-enhanced Raman scattering by tunable, plasmonic gallium nanoparticles, Journal of the American Chemical Society 131 (2009) 12032–12033.
[65] P.C. Wu, M. Losurdo, T.H. Kim, M. Giangregorio, G. Bruno, H.O. Everitt, A.S. Brown, Plasmonic gallium nanoparticles on polar semiconductors: interplay between nanoparticle wetting, localized surface plasmon dynamics, and interface charge, Langmuir 25 (2009) 924–930.
[66] P.C. Wu, T.H. Kim, A.S. Brown, M. Losurdo, G. Bruno, H.O. Everitt, Real-time plasmon resonance tuning of liquid Ga nanoparticles by in situ spectroscopic ellipsometry, Applied Physics Letters 90 (2007) 103119.
[67] K.F. MacDonald, A. Krasavin, N.I. Zheludev, Optical modulation of surface plasmon-polariton coupling in a gallium/aluminium composite, Optics Communications 278 (2007) 207–210.
[68] E.M. Larsson, C. Langhammer, I. Zoric, B. Kasemo, Nanoplasmonic probes of catalytic reactions, Science 326 (2009) 1091–1094.
[69] C. Langhammer, Z. Yuan, I. Zoric, B. Kasemo, Plasmonic properties of supported Pt and Pd nanostructures, Nano Letters 6 (2006) 833–838.
[70] A.K. Sarychev, G. Tartakovsky, Magnetic plasmonic metamaterials in actively pumped host medium and plasmonic nanolaser, Physical Review B 75 (2007) 085436.
[71] C.G. Granqvist, Transparent conductors as solar energy materials: A panoramic review, Solar Energy Materials and Solar Cells 91 (2007) 1529–1598.
[72] M.D. Losego, A.Y. Efremenko, C.L. Rhodes, M.G. Cerruti, S. Franzen, J.P. Maria, Conductive oxide thin films: Model systems for understanding and controlling surface plasmon resonance, Journal of Applied Physics 106 (2009) 024903.
[73] C. Rhodes, M. Cerruti, A. Efremenko, M. Losego, D.E. Aspnes, J.P. Maria, S. Franzen, Dependence of plasmon polaritons on the thickness of indium tin oxide thin films, Journal of Applied Physics 103 (2008) 093108.
[74] C.L. Rhodes, S.H. Brewer, J. Folmer, S. Franzen, Investigation of hexadecanethiol self-assembled monolayers on cadmium tin oxide thin films, Thin Solid Films 516 (2008) 1838–1842.
[75] S. Franzen, Surface plasmon polaritons and screened plasma absorption in indium tin oxide compared to silver and gold, Journal of Physical Chemistry C 112 (2008) 6027–6032.
[76] C. Rhodes, S. Franzen, J.P. Maria, M. Losego, D.N. Leonard, B. Laughlin, G. Duscher, S. Weibel, Surface plasmon resonance in conducting metal oxides, Journal of Applied Physics 100 (2006) 054905.
[77] A. Bostwick, T. Ohta, T. Seyller, K. Horn, E. Rotenberg, Quasiparticle dynamics in graphene, Nature Physics 3 (2007) 36–40.
[78] M. Jablan, H. Buljan, M. Soljacic, Plasmonics in graphene at infrared frequencies, Physical Review B 80 (2009) 245435.
[79] G.W. Hanson, Dyadic Green's functions and guided surface waves for a surface conductivity model of graphene, Journal of Applied Physics 103 (2008) 064302.
[80] R.A. Ferrell, Predicted radiation of plasma oscillations in metal films, Physical Review 111 (1958) 1214–1222.
[81] R.H. Ritchie, Plasma losses by fast electrons in thin films, Physical Review 106 (1957) 874.
[82] A.J. McAlister, E.A. Stern, Plasma resonance absorption in thin metal films, Physical Review 132 (1963) 1599–1602.
[83] D.W. Berreman, Infrared absorption at longitudinal optic frequency in cubic crystal films, Physical Review 130 (1963) 2193.
[84] A. Bichri, J. Lafait, H. Welsch, Visible and infrared optical-properties of Ag/SiO_2 multilayers – radiative virtual modes and coupling effects, J. Phys.-Condes. Matter 5 (1993) 7361–7374.
[85] D.L. Mills, E. Burstein, Polaritons – electromagnetic modes of media, Reports on Progress in Physics 37 (1974) 817–926.
[86] H. Raether, Surface Plasmons on Smooth and Rough Surfaces and on Gratings, Springer Verlag, New York, 1988.
[87] J.M. Pitarke, V.M. Silkin, E.V. Chulkov, P.M. Echenique, Theory of surface plasmons and surface-plasmon polaritons, Reports on Progress in Physics 70 (2007) 1–87.
[88] B. Liedberg, C. Nylander, I. Lundstrom, Surface-plasmon resonance for gas-detection and biosensing, Sensors and Actuators 4 (1983) 299–304.
[89] H. Arwin, M. Poksinski, K. Johansen, Enhancement in ellipsometric thin film sensitivity near surface plasmon resonance conditions, Physica Status Solidi A – Appl. Mat. 205 (2008) 817–820.
[90] V.M. Agranovich, A.A. Maradudin, Surface Polaritons, North Holland Publishing Co., Amsterdam, 1982.
[91] E. Kretschmann, H. Raether, Radiative decay of non radiative surface plasmons excited by light, Zeitschrift Fur Naturforschung Part a-Astrophysik Physik Und Physikalische Chemie A 23 (1968) 2135.
[92] A. Röseler, Spectroscopic infrared ellipsometry, in: H.G. Tompkins, E.A. Irene (Eds.), Handbook of Ellipsometry, William Andrew - Springer, Norwich/Heidelberg, 2005.
[93] F. Abeles, Surface electromagnetic-waves ellipsometry, Surface Science 56 (1976) 237–251.
[94] M. Poksinski, H. Arwin, Protein monolayers monitored by internal reflection ellipsometry, Thin Solid Films 455 (2004) 716–721.
[95] J. Martensson, H. Arwin, H. Nygren, I. Lundstrom, Adsorption and optical-properties of ferritin layers on gold studied with spectroscopic ellipsometry, Journal of Colloid and Interface Science 174 (1995) 79–85.

[96] P. Westphal, A. Bornmann, Biomolecular detection by surface plasmon enhanced ellipsometry, Sensors and Actuators B-Chemical 84 (2002) 278–282.
[97] I.R. Hooper, J.R. Sambles, Sensing using differential surface plasmon ellipsometry, Journal of Applied Physics 96 (2004) 3004–3011.
[98] M. Poksinski, H. Dzuho, J. Järrhed, H. Arwin, in: Eurosensors X 2000, pp. 135.
[99] A.V. Kabashin, V.E. Kochergin, P.I. Nikitin, Surface plasmon resonance bio- and chemical sensors with phase-polarisation contrast, Sensors and Actuators B – Chemical 54 (1999) 51–56.
[100] S.G. Nelson, K.S. Johnston, S.S. Yee, High sensitivity surface plasmon resonance sensor based on phase detection, Sensors and Actuators B – Chemical 35 (1996) 187–191.
[101] A. Nabok, A. Tsargorodskaya, The method of total internal reflection ellipsometry for thin film characterisation and sensing, Thin Solid Films 516 (2008) 8993–9001.
[102] R.M.A. Azzam, Relationship between the P and S Fresnel reflection coefficients of an interface independent of angle of incidence, Journal of the Optical Society of America. A, Optics, Image Science, and Vision 3 (1986) 928–929.
[103] L. Liu, Y.-y. Chen, Y.-h. Meng, S. Chen, G. Jin, Improvement for sensitivity of biosensor with total internal reflection imaging ellipsometry TIRIE, Thin Solid Films 519 (2011) 2758–2762.
[104] A. Nooke, U. Beck, A. Hertwig, A. Krause, H. Kruger, V. Lohse, D. Negendank, J. Steinbach, On the application of gold based SPR sensors for the detection of hazardous gases, Sensors and Actuators B: Chemical 149 (2010) 194–198.
[105] A. Nooke, U. Beck, A. Hertwig, A. Krause, H. Kruger, V. Lohse, D. Negendank, J. Steinbach, Ellipsometric detection of gases with the surface plasmon resonance effect on gold top-coated with sensitive layers, Thin Solid Films 519 (2011) 2659–2663.
[106] J.C.M. Garnett, Colours in metal glasses, in metallic films, and in metallic solutions - II, Philosophical Transactions of the Royal Society of London Series A-Containing Papers of a Mathematical or Physical Character 205 (1906) 237–288.
[107] J.C.M. Garnett, Colours in metal glasses and in metallic films, Philosophical Transactions of the Royal Society of London Series A – Containing Papers of a Mathematical or Physical Character 203 (1904) 385–420.
[108] G. Mie, On the optics of turbid media, especially colloidal metal solutions, Ann. Phys.-Berlin 25 (1908) 377–445.
[109] MiePlot, in: http://www.philiplaven.com/mieplot.htm.
[110] C. Sonnichsen, T. Franzl, T. Wilk, G. von Plessen, J. Feldmann, Plasmon resonances in large noble-metal clusters, New Journal of Physics 4 (2002) 93.
[111] R.H. Doremus, P. Rao, Optical properties of nanosized gold particles, Journal of Materials Research 11 (1996) 2834–2840.
[112] U. Kreibig, Vonfrags.C, Limitation of electron mean free path in small silver particles, Zeitschrift Fur Physik 224 (1969) 307–323.
[113] U. Kreibig, L. Genzel, Optical-absorption of small metallic particles, Surface Science 156 (1985) 678–700.
[114] A. Hilger, M. Tenfelde, U. Kreibig, Silver nanoparticles deposited on dielectric surfaces, Applied Physics B – Lasers and Optics 73 (2001) 361–372.
[115] D. Dalacu, L. Martinu, Spectroellipsometric characterization of plasma-deposited Au/SiO_2 nanocomposite films, Journal of Applied Physics 87 (2000) 228–235.
[116] D. Dalacu, L. Martinu, Spectroellipsometric characterization of plasma-deposited Au fluoropolymer nanocomposite films, J. Vac. Sci. Technol. A – Vac. Surf. Films 17 (1999) 877–883.
[117] T.W.H. Oates, E. Christalle, Real-time spectroscopic ellipsometry of silver nanoparticle formation in poly(vinyl alcohol) thin films, Journal of Physical Chemistry C 111 (2007) 182–187.
[118] T.W.H. Oates, Real time spectroscopic ellipsometry of nanoparticle growth, Applied Physics Letters 88 (2006) 3.
[119] H. Wormeester, A.I. Henry, E.S. Kooij, B. Poelsema, M.P. Pileni, Ellipsometric identification of collective optical properties of silver nanocrystal arrays, Journal of Chemical Physics 124 (2006) 204713.
[120] E.S. Kooij, E.A.M. Brouwer, H. Wormeester, B. Poelsema, Formation and optical characterisation of colloidal gold monolayers, Colloids and Surfaces A – Physicochemical and Engineering Aspects 222 (2003) 103–111.
[121] E.S. Kooij, H. Wormeester, E.A.M. Brouwer, E. van Vroonhoven, A. van Silfhout, B. Poelsema, Optical characterization of thin colloidal gold films by spectroscopic ellipsometry, Langmuir 18 (2002) 4401–4413.
[122] D.E. Aspnes, Plasmonics and effective-medium theories, Thin Solid Films 519 (2011) 2571–2574.
[123] W.K.H. Panofsky, M. Phillips, Classical Electricity and Magnetism, 2nd ed., Addison-Wesley, 1962.
[124] D.E. Aspnes, Local-field effects and effective-medium theory - a microscopic perspective, American Journal of Physics 50 (1982) 704–709.
[125] B. Palpant, B. Prevel, J. Lerme, E. Cottancin, M. Pellarin, M. Treilleux, A. Perez, J.L. Vialle, M. Broyer, Optical properties of gold clusters in the size range 2–4 nm, Physical Review B 57 (1998) 1963–1970.
[126] S. Cho, H. Lim, K.S. Lee, T.S. Lee, B. Cheong, W.M. Kim, S. Lee, Spectro-ellipsometric studies of Au/SiO_2 nanocomposite films, Thin Solid Films 475 (2005) 133–138.
[127] S. Yamaguchi, The resonance type absorption of very thin silver and gold films, Journal of the Physical Society of Japan 15 (1960) 1577–1585.
[128] R.H. Doremus, Optical properties of thin metallic films in Island form, Journal of Applied Physics 37 (1966) 2775–2781.
[129] R. Doremus, Optical absorption of island films of noble metals: wave length of the plasma absorption band, Thin Solid Films 326 (1998) 205–210.
[130] H. Wormeester, E.S. Kooij, B. Poelsema, Effective dielectric response of nanostructured layers, Physica Status Solidi A – Appl. Mat. 205 (2008) 756–763.
[131] H.L. Zhang, S.D. Evans, J.R. Henderson, Spectroscopic ellipsometric evaluation of gold nanoparticle thin films fabricated using layer-by-layer self-assembly, Advanced Materials 15 (2003) 531–534.
[132] N.E. Cant, H.L. Zhang, K. Critchley, T.A. Mykhalyk, G.R. Davies, S.D. Evans, Fabrication and characterization of self-assembled nanoparticle/polyelectrolyte multilayer films, Journal of Physical Chemistry B 107 (2003) 13557–13562.
[133] Z.M. Qi, I. Honma, M. Ichihara, H.S. Zhou, Layer-by-layer fabrication and characterization of gold-nanoparticle/myoglobin nanocomposite films, Advanced Functional Materials 16 (2006) 377–386.
[134] D.A. Brevnov, C. Bungay, Diameter-dependent optical constants of gold mesoparticles electrodeposited on aluminum films containing copper, Journal of Physical Chemistry B 109 (2005) 14529–14535.

[135] H. Pan, S.H. Ko, C.P. Grigoropoulos, Thermal sintering of solution-deposited nanoparticle silver ink films characterized by spectroscopic ellipsometry, Applied Physics Letters 93 (2008) 234104.
[136] M.C. Dixon, T.A. Daniel, M. Hieda, D.M. Smilgies, M.H.W. Chan, D.L. Allara, Preparation, structure, and optical properties of nanoporous gold thin films, Langmuir 23 (2007) 2414–2422.
[137] M.N. Patel, R.D. Williams, R.A. May, H. Uchida, K.J. Stevenson, K.P. Johnston, Electrophoretic deposition of Au nanocrystals inside Perpendicular mesochannels of TiO_2, Chem. Mat. 20 (2008) 6029–6040.
[138] R.A. May, M.N. Patel, K.P. Johnston, K.J. Stevenson, Flow-based multiadsorbate ellipsometric porosimetry for the characterization of mesoporous Pt–TiO_2 and Au–TiO_2 nanocomposites, Langmuir 25 (2009) 4498–4509.
[139] D.H. Wan, H.L. Chen, Y.S. Lin, S.Y. Chuang, J. Shieh, S.H. Chen, Using Spectroscopic Ellipsometry to characterize and apply the optical constants of hollow gold nanoparticles, ACS Nano 3 (2009) 960–970.
[140] T.W.H. Oates, L. Ryves, M.M.M. Bilek, Dielectric functions of a growing silver film determined using dynamic in situ spectroscopic ellipsometry, in: Opt. Express, 2008, pp. 2302-2314.
[141] T. Yamaguchi, S. Yoshida, A. Kinbara, Continuous ellipsometric determination of optical constants and thickness of a silver film during deposition, Japanese Journal of Applied Physics 8 (1969) 559.
[142] H.V. Nguyen, I. An, R.W. Collins, Evolution of the optical functions of thin-film aluminum – a real-time spectroscopic ellipsometry study, Physical Review B 47 (1993) 3947–3965.
[143] H.V. Nguyen, I. An, R.W. Collins, Evolution of the optical functions of aluminum films during nucleation and growth determined by real-time spectroscopic ellipsometry, Physical Review Letters 68 (1992) 994–997.
[144] I.S. An, H. Oh, Optical properties of silver thin films: three-parameter spectroscopic ellipsometry studies, J. Korean Phys. Soc. 29 (1996) 370–376.
[145] T.W.H. Oates, A. Mucklich, Evolution of plasmon resonances during plasma deposition of silver nanoparticles, Nanotechnology 16 (2005) 2606–2611.
[146] T.W.H. Oates, L. Ryves, M.M.M. Bilek, D.R. McKenzie, Accurate determination of optical and electronic properties of ultra-thin silver films for biosensor applications, Sensors and Actuators B – Chemical 109 (2005) 146–152.
[147] K. Mummler, P. Wissmann, Spectroscopic ellipsometry on gold clusters embedded in a Si(111) surface, Thin Solid Films 313 (1998) 522–526.
[148] R.R. Bhat, J. Genzer, Using spectroscopic ellipsometry for quick prediction of number density of nanoparticles bound to non-transparent solid surfaces, Surface Science 596 (2005) 187–196.
[149] T.W.H. Oates, H. Sugime, S. Noda, Combinatorial surface-enhanced raman spectroscopy and spectroscopic ellipsometry of silver island films, Journal of Physical Chemistry C 113 (2009) 4820–4828.
[150] L. Armelao, D. Barreca, G. Bottaro, G. Bruno, A. Gasparotto, A. Losurdo, E. Tondello, RF-sputtering of gold on silica surfaces: evolution from clusters to continuous films, Materials Science & Engineering C – Biomimetic and Supramolecular Systems 25 (2005) 599–603.
[151] J. Toudert, D. Babonneau, L. Simonot, S. Camelio, T. Girardeau, Quantitative modelling of the surface plasmon resonances of metal nanoclusters sandwiched between dielectric layers: the influence of nanocluster, size, shape and organization, Nanotechnology 19 (2008) 125709.
[152] G. Renaud, R. Lazzari, F. Leroy, Probing surface and interface morphology with grazing incidence small angle X-ray scattering, Surface Science Reports 64 (2009) 255–380.
[153] D.A.G. Bruggeman, Calculation of various physics constants in heterogenous substances I Dielectricity constants and conductivity of mixed bodies from isotropic substances, Ann. Phys.-Berlin 24 (1935) 636–664.
[154] A.C. Galca, E.S. Kooij, H. Wormeester, C. Salm, V. Leca, J.H. Rector, B. Poelsema, Structural and optical characterization of porous anodic aluminum oxide, Journal of Applied Physics 94 (2003) 4296–4305.
[155] C.G. Granqvist, O. Hunderi, Optical-properties of Ag–SiO_2 Cermet films – comparison of effective-medium theories, Physical Review B 18 (1978) 2897–2906.
[156] G.B. Smith, A.I. Maaroof, M.B. Cortie, Percolation in nanoporous gold and the principle of universality for two-dimensional to hyperdimensional networks, Physical Review B 78 (2008) 165418.
[157] F. Bisio, M. Palombo, M. Prato, O. Cavalleri, E. Barborini, S. Vinati, M. Franchi, L. Mattera, M. Canepa, Optical properties of cluster-assembled nanoporous gold films, Physical Review B 80 (2009) 205428.
[158] M. Hovel, B. Gompf, M. Dressel, Dielectric properties of ultrathin metal films around the percolation threshold, Physical Review B 81 (2010) 035402.
[159] R. Gans, The shape of ultra microscopic gold particles, Ann. Phys.-Berlin 37 (1912) 881–900.
[160] J. Perez-Juste, I. Pastoriza-Santos, L.M. Liz-Marzan, P. Mulvaney, Gold nanorods: synthesis, characterization and applications, Coordination Chemistry Reviews 249 (2005) 1870–1901.
[161] J.M. Lamarre, Z. Yu, C. Harkati, S. Roorda, L. Martinu, Optical and microstructural properties of nanocomposite Au/SiO_2 films by containing particles deformed by heavy ion irradiation, Thin Solid Films 479 (2005) 232–237.
[162] E. Prodan, C. Radloff, N.J. Halas, P. Nordlander, A hybridization model for the plasmon response of complex nanostructures, Science 302 (2003) 419–422.
[163] J.C.M. Garnett, Colours in metal glasses and in metallic films, Philosophical Transactions, Series A 203 (1904) 385–420.
[164] S. Yamaguchi, Optical absorption of heat treated very thin silver films and its dependence on angle of incidence, Journal of the Physical Society of Japan 17 (1962) 1172.
[165] P. Royer, J.P. Goudonnet, R.J. Warmack, T.L. Ferrell, Substrate effects on surface-plasmon spectra in metal-island films, Physical Review B 35 (1987) 3753–3759.
[166] T. Yamaguchi, A. Kinbara, Optical effect of substrate on plasma resonance-absorption of an aggregated silver film, Japanese Journal of Applied Physics 2 (1974) 677–680.
[167] T. Yamaguchi, S. Yoshida, A. Kinbara, Effect of retarded dipole-dipole interactions between island particles on optical plasma-resonance absorption of a silver-island film, Journal of the Optical Society of America 64 (1974) 1563–1568.
[168] L.A.A. Pettersson, F. Carlsson, O. Inganäs, H. Arwin, Spectroscopic ellipsometry studies of the optical properties of doped poly(3,4-ethylenedioxythiophene): an anisotropic metal, Thin Solid Films 313–314 (1998) 356–361.
[169] T. Yamaguchi, S. Yoshida, A. Kinbara, Anomalous optical-absorption of aggregated silver films, Thin Solid Films 18 (1973) 63–70.

[170] V.V. Truong, R. Belley, G. Bader, A. Hache, Spectroscopic multiple angle reflection and transmission ellipsometry of aggregated gold films, Applied Surface Science 212 (2003) 140–145.
[171] D. Bedeaux, J. Vlieger, Phenomenological theory of dielectric properties of thin-films, Physica 67 (1973) 55–73.
[172] D. Bedeaux, J. Vlieger, Optical Properties of Surfaces, Imperial College Press, 2001.
[173] M.T. Haarmans, D. Bedeaux, The polarizability and the optical-properties of lattices and random distributions of small metal spheres on a substrate, Thin Solid Films 224 (1993) 117–131.
[174] R. Lazzari, I. Simonsen, GRANFILM: a software for calculating thin-layer dielectric properties and Fresnel coefficients, Thin Solid Films 419 (2002) 124–136.
[175] R.G. Barrera, M. Delcastillomussot, G. Monsivais, P. Villasenor, W.L. Mochan, Optical-properties of 2-dimensional disordered-systems on a Substrate, Physical Review B 43 (1991) 13819–13826.
[176] M.T. Haarmans, D. Bedeaux, Optical-properties of thin-films up to 2nd-order in the thickness, Thin Solid Films 258 (1995) 213–223.
[177] A.C. Rijn van Alkemade, Ph.D. thesis, in: University of Leiden, Leiden, 1881.
[178] J. Lekner, Theory of Reflection, Martinus Nijhof Publishers, Dordrecht, 1987.
[179] M.R. Bohmer, E.A. van der Zeeuw, G.J.M. Koper, Kinetics of particle adsorption in stagnation point flow studied by optical reflectometry, Journal of Colloid and Interface Science 197 (1998) 242–250.
[180] A.J. de Vries, E.S. Kooij, H. Wormeester, A.A. Mewe, B. Poelsema, Ellipsometric study of percolation in electroless deposited silver films, Journal of Applied Physics 101 (2007) 053703.
[181] H. Wormeester, E.S. Kooij, A. Mewe, S. Rekveld, B. Poelsema, Ellipsometric characterisation of heterogeneous 2D layers, Thin Solid Films 455 (2004) 323–334.
[182] E.S. Kooij, H. Wormeester, A.C. Galca, B. Poelsema, Optical anisotropy and porosity of anodic aluminum oxide characterized by spectroscopic ellipsometry, Electrochemical and Solid State Letters 6 (2003) B52–B54.
[183] R. Lazzari, G. Renaud, C. Revenant, J. Jupille, Y. Borensztein, Adhesion of growing nanoparticles at a glance: Surface differential reflectivity spectroscopy and grazing incidence small angle X-ray scattering, Physical Review B 79 (2009) 125428.
[184] G. Renaud, R. Lazzari, C. Revenant, A. Barbier, M. Noblet, O. Ulrich, F. Leroy, J. Jupille, Y. Borensztein, C.R. Henry, J.P. Deville, F. Scheurer, J. Mane-Mane, O. Fruchart, Real-time monitoring of growing nanoparticles, Science 300 (2003) 1416–1419.
[185] J.B. Pendry, A.J. Holden, D.J. Robbins, W.J. Stewart, Magnetism from conductors and enhanced nonlinear phenomena, IEEE Transactions on Microwave Theory and Techniques 47 (1999) 2075–2084.
[186] V.G. Veselago, Electrodynamics of substances with simultaneously negative values of sigma and Mu, Soviet Physics Uspekhi-Ussr 10 (1968) 509–514.
[187] J.B. Pendry, Negative refraction makes a perfect lens, Physical Review Letters 85 (2000) 3966–3969.
[188] D.R. Smith, W.J. Padilla, D.C. Vier, S.C. Nemat-Nasser, S. Schultz, Composite medium with simultaneously negative permeability and permittivity, Physical Review Letters 84 (2000) 4184–4187.
[189] W. Cai, V.M. Shalaev, Optical Metamaterials: Fundamentals and Applications, Springer, 2010.
[190] S.A. Ramakrishna, T.M. Grzegorczyk, Negative Refractive Index Materials, SPIE Press, Washington, 2009.
[191] Physics of Negative Refraction and Negative Index Material, Springer, 2007.
[192] Y. Zhang, B. Fluegel, A. Mascarenhas, Total negative refraction in real crystals for ballistic electrons and light, Physical Review Letters 91 (2003) 157404.
[193] A.J. Hoffman, L. Alekseyev, S.S. Howard, K.J. Franz, D. Wasserman, V.A. Podolskiy, E.E. Narimanov, D.L. Sivco, C. Gmachl, Negative refraction in semiconductor metamaterials, Nature Materials 6 (2007) 946–950.
[194] J. Yao, Z.W. Liu, Y.M. Liu, Y. Wang, C. Sun, G. Bartal, A.M. Stacy, X. Zhang, Optical negative refraction in bulk metamaterials of nanowires, Science 321 (2008) 930.
[195] D.R. Smith, D. Schurig, Electromagnetic wave propagation in media with indefinite permittivity and permeability tensors, Physical Review Letters 90 (2003) 077405.
[196] A. Fang, T. Koschny, C.M. Soukoulis, Optical anisotropic metamaterials: Negative refraction and focusing, Physical Review B 79 (2009) 245127.
[197] P.A. Belov, R. Marques, S.I. Maslovski, I.S. Nefedov, M. Silveirinha, C.R. Simovski, S.A. Tretyakov, Strong spatial dispersion in wire media in the very large wavelength limit, Physical Review B 67 (2003) 113103.
[198] J.B. Pendry, A.J. Holden, W.J. Stewart, I. Youngs, Extremely low frequency plasmons in metallic mesostructures, Physical Review Letters 76 (1996) 4773–4776.
[199] T.W.H. Oates, A. Keller, S. Facsko, A. Mucklich, Aligned silver nanoparticles on rippled silicon templates exhibiting anisotropic plasmon absorption, Plasmonics 2 (2007) 47–50.
[200] M. Ranjan, T.W.H. Oates, S. Facsko, W. Möller, Optical properties of silver nanowire arrays with 35 nm periodicity, Optics Letters 35 (2010) 2576–2578.
[201] T.W.H. Oates, M. Ranjan, S. Facsko, H. Arwin, Highly anisotropic effective dielectric functions of silver nanoparticle arrays, Optics Express 19 (2011) 2014–2028.
[202] J. Humlicek, Infrared resonances of local fields and ellipsometric spectra of negative refraction metamaterials, Thin Solid Films 519 (2011) 2655–2658.
[203] K.F. Lindmann, Über eine durch ein isotropes System von spiralförmigen Resonatoren erzeugte Rotationspolarisation der elekromagnetischen Wellen, Annalen Der Physik, Leipzig 63 (1920) 621.
[204] D.R. Smith, S. Schultz, P. Markos, C.M. Soukoulis, Determination of effective permittivity and permeability of metamaterials from reflection and transmission coefficients, Physical Review B 65 (2002) 195104.
[205] C. Menzel, T. Paul, C. Rockstuhl, T. Pertsch, S. Tretyakov, F. Lederer, Validity of effective material parameters for optical fishnet metamaterials, Physical Review B 81 (2010) 035320.
[206] T.J. Yen, W.J. Padilla, N. Fang, D.C. Vier, D.R. Smith, J.B. Pendry, D.N. Basov, X. Zhang, Terahertz magnetic response from artificial materials, Science 303 (2004) 1494–1496.
[207] R. Marques, F. Medina, R. Rafii-El-Idrissi, Role of bianisotropy in negative permeability and left-handed metamaterials, Physical Review B 65 (2002) 144440.

[208] P.D. Rogers, T.D. Kang, T. Zhou, M. Kotelyanskii, A.A. Sirenko, Mueller matrices for anisotropic metamaterials generated using 4×4 matrix formalism, Thin Solid Films 519 (2011) 2668–2673.
[209] S. Linden, C. Enkrich, M. Wegener, J.F. Zhou, T. Koschny, C.M. Soukoulis, Magnetic response of metamaterials at 100 terahertz, Science 306 (2004) 1351–1353.
[210] J. Parsons, E. Hendry, J.R. Sambles, W.L. Barnes, Localized surface-plasmon resonances and negative refractive index in nanostructured electromagnetic metamaterials, Physical Review B 80 (2009) 6.
[211] M.W. Klein, C. Enkrich, M. Wegener, C.M. Soukoulis, S. Linden, Single-slit split-ring resonators at optical frequencies: limits of size scaling, Optics Letters 31 (2006) 1259–1261.
[212] M. Jakovljevic, G. Isic, B. Vasic, R. Gajic, T.W.H. Oates, K. Hinrichs, I. Bergmair, K. Hingerl, Characterization of split-ring resonators using spectroscopic ellispometry, in: Metamaterials, Barcelona, 2011.
[213] C. Rockstuhl, F. Lederer, C. Etrich, T. Zentgraf, J. Kuhl, H. Giessen, On the reinterpretation of resonances in split-ring-resonators at normal incidence, Optics Express 14 (2006) 8827–8836.
[214] G. Isic, B. Vasic, M. Miric, B. Jokanovic, I. Bergmair, Modelling the variable angle reflection and transmission from metamaterial slabs, Acta Physica Polonica A 116 (2009) 631.
[215] V.A. Podolskiy, A.K. Sarychev, V.M. Shalaev, Plasmon modes and negative refraction in metal nanowire composites, Optics Express 11 (2003) 735–745.
[216] V.M. Shalaev, W.S. Cai, U.K. Chettiar, H.K. Yuan, A.K. Sarychev, V.P. Drachev, A.V. Kildishev, Negative index of refraction in optical metamaterials, Optics Letters 30 (2005) 3356–3358.
[217] S. Zhang, W.J. Fan, K.J. Malloy, S.R.J. Brueck, N.C. Panoiu, R.M. Osgood, Near-infrared double negative metamaterials, Optics Express 13 (2005) 4922–4930.
[218] S. Zhang, W.J. Fan, N.C. Panoiu, K.J. Malloy, R.M. Osgood, S.R.J. Brueck, Experimental demonstration of near-infrared negative-index metamaterials, Physical Review Letters 95 (2005) 4.
[219] G. Dolling, C. Enkrich, M. Wegener, C.M. Soukoulis, S. Linden, Simultaneous negative phase and group velocity of light in a metamaterial, Science 312 (2006) 892–894.
[220] G. Dolling, M. Wegener, C.M. Soukoulis, S. Linden, Negative-index metamaterial at 780 nm wavelength, Optics Letters 32 (2007) 53–55.
[221] T.W.H. Oates, B. Dastmalchi, K. Hingerl, I. Bergmair, K. Hinrichs, Characterizing metamaterials using spectroscopic ellipsometry in: The Fifth International Congress on Advanced Electromagnetic Materials in Microwaves and Optics, Barcelona, 2011.
[222] V.M. Agranovich, Y.N. Gartstein, Spatial dispersion and negative refraction of light, Physics-Uspekhi 49 (2006) 1029–1044.
[223] V.M. Agranovich, Y.N. Gartstein, Spatial dispersion, polaritons and negative refraction, in: C.M. Krowne, Y. Zhang (Eds.), Physics of Negative Refraction and Negative Index Materials, Springer, 2007.
[224] J.B. Pendry, A chiral route to negative refraction, Science 306 (2004) 1353–1355.
[225] S. Tretyakov, I. Nefedov, A. Sihvola, S. Maslovski, C. Simovski, Waves and energy in chiral nihility, Journal of Electromagnetic Waves and Applications 17 (2003) 695–706.
[226] J.H. Freudenthal, E. Hollis, B. Kahr, Imaging Chiroptical Artifacts, Chirality 21 (2010) E20–E27.
[227] J.N. Hilfiker, C.M. Herzinger, T. Wagner, A. Marino, G. Delgais, G. Abbate, Mueller-matrix characterization of liquid crystals, Thin Solid Films 455 (2004) 591–595.
[228] R. Ossikovski, M. Anastasiadou, S. Ben Hatit, E. Garcia-Caurel, A. De Martino, Depolarizing Mueller matrices: how to decompose them?, Physica Status Solidi A – Applied Materials 205 (2008) 720–727
[229] R.M.A. Azzam, Chiral Thin Solid Films - Method of Deposition and Applications, Applied Physics Letters 61 (1992) 3118–3120.
[230] B. Gallas, N. Guth, J. Rivory, H. Arwin, R.G. Magnusson, G., J. Yang, K. Robbie, Nanostructured chiral silver thin films: A route to metamaterials at optical frequencies, Thin Solid Films 519 (2011) 2650–2654.
[231] T.W. Ebbesen, H.J. Lezec, H.F. Ghaemi, T. Thio, P.A. Wolff, Extraordinary optical transmission through sub-wavelength hole arrays, Nature 391 (1998) 667–669.
[232] W.L. Barnes, A. Dereux, T.W. Ebbesen, Surface plasmon subwavelength optics, Nature 424 (2003) 824–830.
[233] J. Braun, B. Gompf, G. Kobiela, M. Dressel, How holes can obscure the view: suppressed transmission through an ultrathin metal film by a subwavelength hole array, Physical Review Letters 103 (2009) 203901.
[234] B. Gompf, J. Braun, T. Weiss, H. Giessen, M. Dressel, H.U., Periodic nanostructures: spatial dispersion mimics chirality, Phys. Rev. Lett., in press.